Design and validation of an unmanned surface vehicle simulation model

Peter H. Heins[a,*], Bryn Ll. Jones[a], Dominic J. Taunton[b]

[a]*Department of Automatic Control and Systems Engineering, The University of Sheffield, Sheffield, U.K.*
[b]*Engineering and the Environment, University of Southampton, Southampton, U.K.*

Abstract

In this paper we present a multiphysics simulation model of Halcyon, an autonomous unmanned surface vehicle (USV). The simulation model presented in this paper has been developed to rapidly progress the design, development and validation of Halcyon's autonomy management system, particularly in challenging sea conditions. Using simulation for this purpose enables extensive testing across the full environmental operating envelope of the vessel, hence greatly reducing the need for real-world sea-trials. The simulator is comprised of a novel and comprehensive sea-surface wave environment model, a six degree of freedom nonlinear unified seakeeping and manoeuvring boat dynamics model, an actuation dynamics model, an autopilot and an interface with an autonomy management system. Results are presented that show good agreement between real-world and simulated sea-trials data.

Keywords: multiphysics, ship modelling, wave modelling, simulation, model validation

1. Introduction

Unmanned surface vehicles (USVs) are autonomous marine craft that operate on the surface of a body of water without any personnel onboard. They are analogous to airborne unmanned aerial vehicles (UAVs) and subaquatic unmanned underwater vehicles (UUVs) [1]. USVs have been widely used to conduct scientific research in the fields of oceanography [2] and meteorology [3] and have their applications in the oil and gas industry also. Within the Defence sector, USVs are currently being developed for several roles including anti-submarine warfare and minesweeping. One such USV is *Halcyon* which is currently being developed by Thales UK and ASV Global for autonomous mine clearing missions. The simulation model presented in this paper has been developed to aid in the development, testing and validation of Halcyon's autonomy management system. Using simulation for this purpose reduces the need to conduct time-consuming and expensive sea-trials and allows for greater flexibility over the environmental conditions in which the boat must operate. This flexibility offers the additional advantage of being able to test and evaluate several guidance, navigation and control (GNC) systems using the same "random" wave environment. To aid in this, the simulator incorporates a novel sea-surface wave environment model which is an integration of

---

*Corresponding author
Email addresses:* `p.heins@sheffield.ac.uk` (Peter H. Heins), `b.l.jones@sheffield.ac.uk` (Bryn Ll. Jones), `djt2@soton.ac.uk` (Dominic J. Taunton)
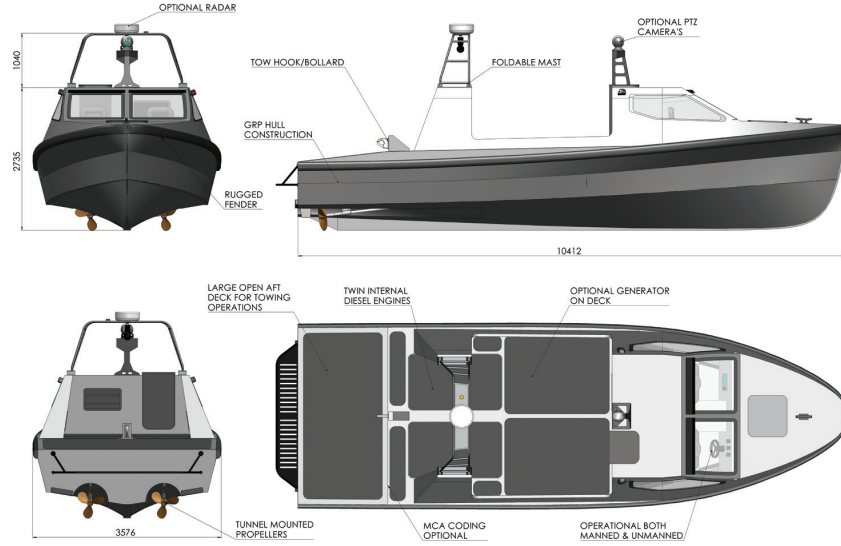
Figure 1: Drawings of Halcyon.

several spectral wave models and is capable of simulating omnidirectional surface waves produced or affected by ocean swell, local wind, surface currents and finite water depth.

Drawings of Halcyon are shown in Figure 1 and a brief technical specification is given in Table 1. The craft's hydrodynamic parameters, which determine the various forces imparted upon the vessel from the surrounding water, depend heavily on the geometry of the hull and the boat's mass distribution. In the current work, these are calculated using the hydrodynamic code THARBM [4]. Model parameters that are unknown a priori are identified by comparing simulation output to sea-trials data for Halcyon.

The overarching objective of the simulation model is to provide a physics-based platform for rapidly developing and evaluating a USV's autonomy management system. This means that in designing the simulation model, a compromise must be struck between the efficiency of evaluation, in order that simulations can be ran in real-time, and the accuracy of the solution. With this in mind, the simulation model need only retain the key physics sufficient to achieve good qualitative agreement with the sea-trials data.

Modern USVs vary in their shape, size and configuration. Smaller USVs which are $O(10^{-1})$-$O(10^0)$ metres in length, tend to be deployed mainly for scientific research [5] as well as for security monitoring [6]. Larger USVs which are $O(10^1)$ metres in length are used in a wider variety of roles including Defence-based roles. Halcyon, being $O(10^1)$ metres in length and having a "patrol boat" hull form, is representative of a wide array of medium-to-large sized USVs which are currently being developed by the Defence industry. Therefore, given a full set of rigid body and hydrodynamic data, the model presented in the following could be quickly parameterised to simulate the dynamics of many current or future USVs.

Examples of other USV simulation models can be found in the literature. Many, if not all, of these models include manoeuvring dynamics only in order to design and test GNC systems [7, 8, 9, 10, 11]. By not accounting for the seakeeping dynamics, these models are only applicable to marine

Parameter	Symbol	Value	Unit
Length overall	L_{oa}	11.2	metres
Beam	B	3.2	metres
Height overall	H_{oa}	2.9	metres
Draft	T	0.7	metres
Mass	m	11000	kilograms
Top Speed		25	knots
No. of engines		2	
No. of rudders		2	

Table 1: Halcyon's technical specifications.

craft navigating in calm waters. To the best of the authors' knowledge, the USV simulation model outlined in this paper is the first to rigorously account for wind and wave-induced forces and is therefore applicable to a wider range of sea conditions.

The remainder of this paper is organised as follows. An overview of the simulation model and its major components is given in Section 2, the novel wave environment model is presented in Section 3, the reference frames used to derive the simulation model are outlined in Section 4, the six degree of freedom rigid body dynamics model is presented in Section 5, Section 6 outlines the actuation dynamics model, the autopilot and autonomy management system interface are discussed in Section 7, Section 8 presents the sea-trials validation and model tuning exercise, and finally concluding remarks are given in Section 9.

2. Overview of the simulation model

The simulation model consists of five major components: a six degree of freedom boat dynamics model, an actuation dynamics model, a wave environment model, an interface with the autonomy management system and an autopilot. These are illustrated in Figure 2.

A six degree of freedom nonlinear unified seakeeping and manoeuvring model with fluid memory effects [12] is used to model the inertial motions of Halcyon. Speed-dependent damping and hydrodynamic added-mass are included in this model. Wave-induced forces are modelled as a set of speed-dependent response amplitude operator (RAO) data which have been calculated using a hydrodynamic code based upon the hull geometry. Models for Halcyon's rudders, propellers and engines have also been developed to accurately simulate the vessel's actuation dynamics.

Besides the boat dynamics model, a multiphysics wave environment model has been developed to simulate dynamic environmental disturbances. This model generates omnidirectional surface waves produced from the combined effects of gusting local wind, ocean swell, surface current and finite water depth. This is achieved by integrating several semi-empirical spectral models.

Halcyon's autonomy management system is implemented in MOOS-IvP [13], an open-source autonomy architecture for unmanned vehicles. MOOS-IvP solves multi-objective optimisation problems based on competing behaviours to determine how a mission should be executed. Behaviours are separate control/mission objectives such as navigating to a waypoint or object collision avoidance and require certain sensor data to be sent from Halcyon such as GPS position. MOOS-IvP sends desired speed and heading information in return. The simulation model includes an interface with MOOS-IvP such that the simulation can run in feedback with the autonomy management system over a network in real time. An autopilot, included in the simulation model, determines
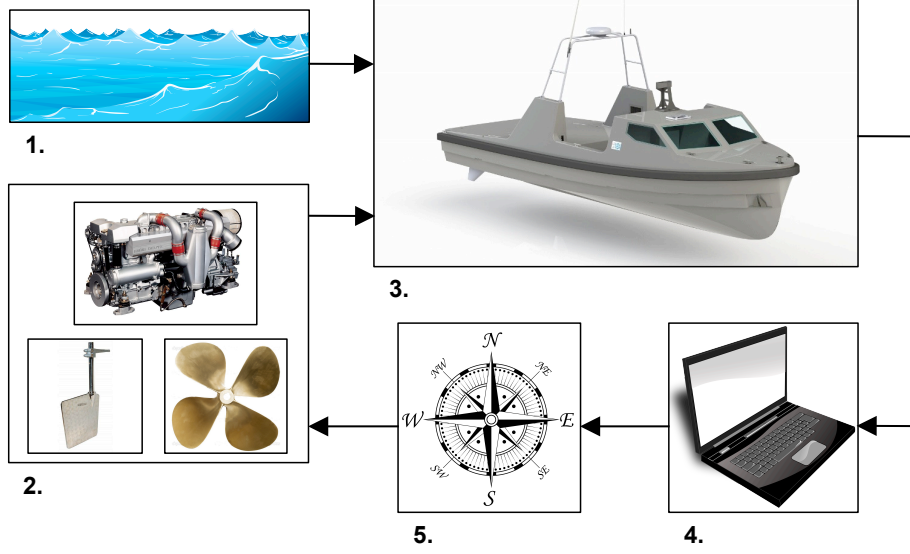
Figure 2: A diagram showing the interactions between the simulation model's components: 1. Wave environment model, 2. Actuation dynamics model, 3. Boat dynamics model, 4. Autonomy management system interface, 5. Autopilot.

thrust and rudder settings based on the desired speed and heading information sent by MOOS-IvP. The autopilot consists of three proportional-integral-differential (PID) controllers which have been tuned specifically for Halcyon.

3. Wave Environment Model

Relatively lightweight vessels, such as Halcyon, experience significant perturbations in all six degrees of freedom due to the hydrodynamic forces imparted from the surrounding waves. It is therefore imperative that surface waves and their interactions with a moving vessel are modelled appropriately.

The first-order wave-induced forces experienced by a vessel, $\tau_{\text{wave}} \in \mathbb{R}^6$, are calculated as [14]:

$$\tau_{\text{wave}}^{\{\text{dof}\}} = \sum_{i=1}^{N} \sum_{j=1}^{M} \rho_{\text{w}} g \left| F_{\text{wave}}^{\{\text{dof}\}}(U, k_{\text{i}}, \theta_{\text{j}}) \right| A_{k_{\text{i}}, \theta_{\text{j}}} \cos \left(\omega_{\text{e}}(U, k_{\text{i}}, \theta_{\text{j}}) t + \angle F_{\text{wave}}^{\{\text{dof}\}}(k_{\text{i}}, \theta_{\text{j}}) + \epsilon_{k_{\text{i}}} \right), \quad (1)$$

where dof $\in \{1, 2, 3, 4, 5, 6\}$, $\rho_{\text{w}} = 1025$ kg/m^3 is the density of seawater, $g = 9.81$ m/s^2 is acceleration due to gravity, $F_{\text{wave}} \in \mathbb{C}^6$ are complex-valued normalised force response amplitude operators (RAOs) and $A_{k_{\text{i}}, \theta_{\text{j}}} \in \mathbb{R}$ is the amplitude of a wave with spatial wavenumber $k_{\text{i}} \in \mathbb{R}$ and direction $\theta_{\text{j}} \in \mathbb{R}$. Lastly, $\epsilon_{k_{\text{i}}} \in [0, 2\pi]$ is a random added phase component, and encounter frequency, $\omega_e \in \mathbb{R}$, is defined:

$$\omega_{\text{e}}(U, k_{\text{i}}, \theta_{\text{j}}) := \omega_{\text{i}} - \frac{\omega_{\text{i}}^2}{g} U \cos(\theta_{\text{j}}), \quad (2)$$

where $U \in \mathbb{R}$ denotes forward speed, angular frequency is defined via the linear dispersion relation as $\omega_{\text{i}}^2 := g k_{\text{i}} \tanh(k_{\text{i}} d)$ [15] and $d \in \mathbb{R}$ denotes water depth.
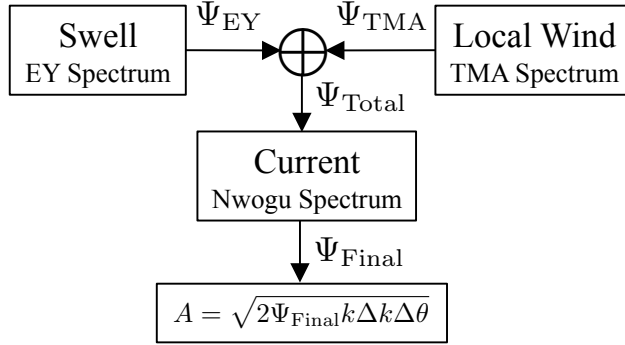
Figure 3: Schematic of how wave amplitudes are generated in the wave environment model.

The wave environment model computes the wave amplitudes, A_{k_i, θ_j}, from a combination of spectral wave models (SWMs) which model the effects of ocean swell, local wind, surface current and finite water depth. For a given set of inputs such as, for instance, water depth and windspeed, each SWM produces a continuous omnidirectional wave energy spectrum $\Psi(k, \theta) \in \mathbb{R}$. In the wave environment model, Elfouhaily (EY) [16] and Texel-MARSEN-ARSLOE (TMA) [17] spectra are superimposed to produce a total continuous wave energy spectrum: $\Psi_{\text{Total}} = \Psi_{\text{EY}} + \Psi_{\text{TMA}}$. This is analogous to the Torsethaugen [18] and Ochi-Hubble [19] multi-peak SWMs which have low-frequency (ocean swell) and high frequency (local wind) spectral peaks. However, neither the Torsethaugen or Ochi-Hubble SWMs include the effects of finite water depth. The total wave energy spectrum is then multiplied by Nwogu's current influence spectrum [20], $C(k, \theta) \in \mathbb{R}$, to produce the final continuous wave energy spectrum:

$$\Psi_{\text{Final}}(k, \theta) = C(k, \theta) \circ \Psi_{\text{Total}}(k, \theta), \tag{3}$$

where $\circ$ denotes a Hadamard dot product. The discrete wave amplitudes are calculated from (3) as:

$$A_{k_i, \theta_j} = \sqrt{2\Psi_{\text{Final}}(k_i, \theta_j)k_i \Delta k \Delta \theta}, \tag{4}$$

where $\Delta k := |k_{i+1} - k_i|$ and $\Delta \theta := |\theta_{j+1} - \theta_j|$. A schematic showing how wave amplitudes are generated is shown in Figure 3.

All omnidirectional SWMs have the form:

$$\Psi(k, \theta) = S(k)D(k, \theta), \tag{5}$$

where $S(k) \in \mathbb{R}$ is termed the unidirectional wave spectrum, and $D(k, \theta) \in \mathbb{R}$ is called the spreading function. $S(k)$ dictates the amount of energy that is contained in the waves' spatial frequencies, and can be used alone to reconstruct unidirectional surface waves. $D(k, \theta)$ is required to spread the wave energy to waves travelling in directions other than the principle wave direction. The SWMs used in the wave environment model will be outlined in the following sections.

3.1. Elfouhaily (EY) spectrum

The EY omnidirectional SWM [16] is used to model the effects of ocean swell. It was developed by unifying the results from several pre-existing SWMs into one model, and it is widely used for

ocean surface modelling [21, 22]. For the EY spectrum, $S(k)$ is comprised of a low-frequency wave spectrum, a modified JONSWAP spectrum [23], and a high-frequency wave spectrum. It incorporates a spreading function which ensures long waves are aligned with the principle wind direction and short waves are more directional; something witnessed from radar observations [16]. The EY SWM is given as [16]:

$$\Psi_{\text{EY}}(k, \theta, \Lambda_{\text{EY}}) = \frac{1}{2\pi} k^{-4} \left[B_l(k, \Lambda_{\text{EY}}) + B_h(k, \Lambda_{\text{EY}}) \right] D_{\text{EY}}(k, \theta, \Lambda_{\text{EY}}), \tag{6}$$

where parameter vector $\Lambda_{\text{EY}} = \begin{bmatrix} U_s & x_f & \beta_s \end{bmatrix}^\top$, U_s is swell windspeed 10 metres above sea level, x_F is fetch in metres and β_s is the principle swell direction.

The low-frequency spectral components are modelled as:

$$B_l(k, \Lambda_{\text{EY}}) = \frac{1}{2} \alpha_p \frac{c_p}{c} F_p, \tag{7}$$

where,

$$\alpha_p = 6 \times 10^{-3} \sqrt{\Omega}, \quad \Omega = U_s/c_p = 0.84 \tanh\left\{ (X/X_0)^{0.4} \right\}^{-0.75},$$

$$c_p = c(k_p), \quad k_p = k_0 \Omega^2, \quad k_0 = g/U_s^2,$$

$$c = \omega/k, \quad X = k_0 x_F, \quad X_0 = 2.2 \times 10^4,$$

$$F_p = L_{\text{PM}} J_p \exp\left\{ -\frac{\Omega}{\sqrt{10}} \left[\sqrt{\frac{k}{k_p}} - 1 \right] \right\}, \quad L_{\text{PM}} = \exp\left\{ -\frac{5}{4}(k_p/k)^2 \right\},$$

$$J_p = \gamma^\Gamma, \quad \Gamma = \exp\left\{ -\frac{\left(\sqrt{\frac{k}{k_p}} - 1 \right)^2}{2\sigma^2} \right\}, \quad \sigma = 0.08 \left[1 + 4\Omega^{-3} \right],$$

$$\gamma = \begin{cases} 1.7 & 0.84 < \Omega < 1 \\ 1.7 + 6\log(\Omega) & 1 < \Omega < 5 \end{cases},$$

Ω is dimensionless inverse wave age and c is wave phase speed.

The high-frequency spectral components are modelled as:

$$B_h(k, \Lambda_{\text{EY}}) = \frac{1}{2} \alpha_m \frac{c_m}{c} F_m, \tag{8}$$

where,

$$\alpha_m = 10^{-2} \begin{cases} 1 + \ln(u^*/c_m) & \text{for } u^* < c_m \\ 1 + 3\ln(u^*/c_m) & \text{for } u^* > c_m \end{cases}, \quad c_m = c(k_m) = 0.23 m/s,$$

$$u^* = \sqrt{C_{DN}} U_s, \quad C_{DN} = 5.1 \times 10^{-4} U_s^{0.46},$$

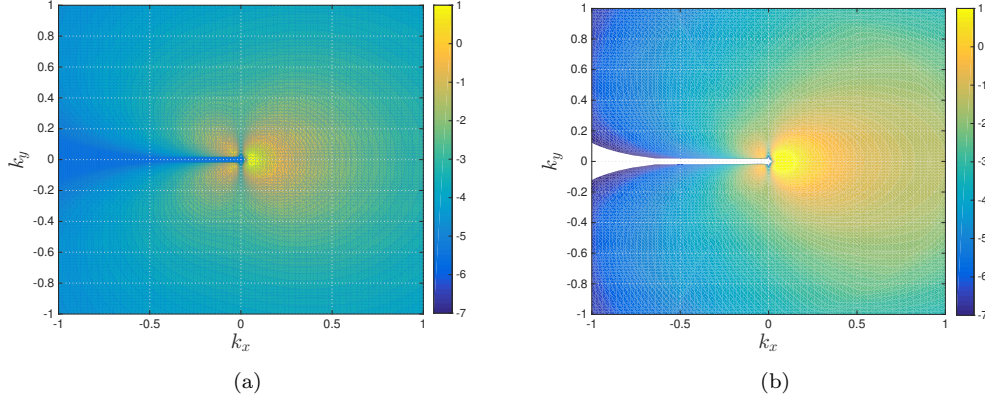$$F_m = \exp\left\{ -\frac{1}{4} \left[\frac{k}{k_m} - 1 \right]^2 \right\},$$

6

Figure 4: Contour plots of: (a) $\log_{10} \Psi_{EY}(k_x = k\cos(\theta), k_y = k\sin(\theta))$ for southerly swell windspeed 10m/s, 10^4 km fetch, Sea State 4 and (b) $\log_{10} \hat{\Psi}_{EY}$ for northerly surface current speed $U_c = 2$m/s, southerly swell windspeed 10m/s, 10^4 km fetch and corresponding to Sea State 5.

and u^* is the friction velocity at the water surface.

The spreading function used in the EY SWM is given as:

$$D_{EY}(k, \theta, \Lambda_{EY}) = [1 + \Delta(k)\cos(2\{\theta + \beta_s\})] \left[\frac{\cos(\theta + \beta_s)}{2} \right]^2, \tag{9}$$

where,

$$\Delta(k) = \tanh\left\{ a_0 + a_p(c/c_p)^{2.5} + a_m(c_m/c)^{2.5} \right\},$$

$$a_0 = \frac{\ln(2)}{2}, \quad a_p = 4, \quad a_m = 0.13\frac{u^*}{c_m}.$$

An example EY spectrum is plotted in Figure 4(a). It can be seen that the EY spectrum is highly directional with a significant portion of energy given to waves travelling in directions far from the principle wind direction. Note that in the plot, $k_x = k\cos(\theta)$ is a North-facing wavenumber vector and $k_y = k\sin(\theta)$ is an East-facing wavenumber vector. Figure 5(a) is a sea-surface elevation (η) plot produced using the spectrum shown in Figure 4(a). The high directionality of the waves are easier to visualise in this plot.

Note that in Figures 5(a), 5(b) and 7 a large number of waves are used to produce the sea-surface elevation plots. This is for illustrative purposes only. The number of individual waves that are included in the USV simulation model is typically much smaller. For instance, the number of waves that were included in the simulations presented in Section 8 was 32^2. This was enough to capture the non-negligible wave-induced forces.

3.2. Texel-MARSEN-ARSLOE (TMA) spectrum

The TMA SWM [17] is used to model the effects of local wind and finite water depth on the waves' amplitudes. This model is a unidirectional JONSWAP spectrum [23] which has been modified to include the effects of finite water depth. For a given set of input parameters, the peak
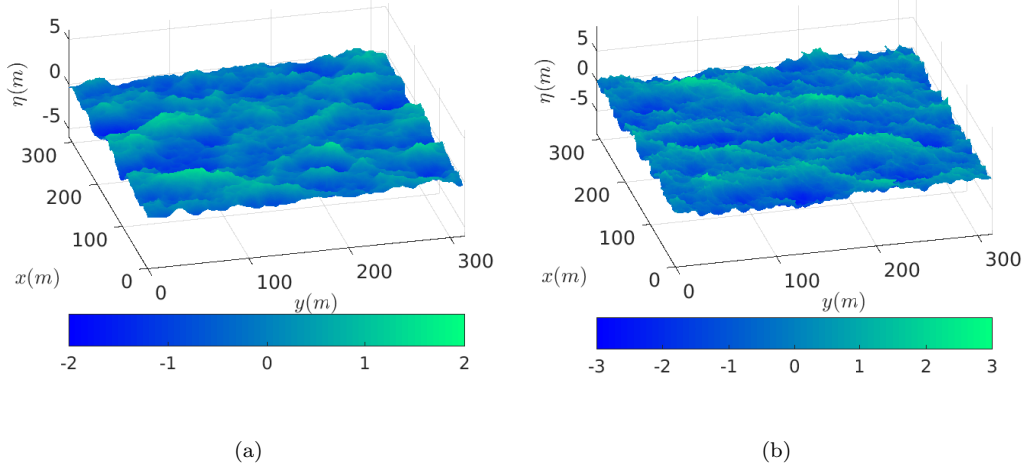
7

Figure 5: Sea-surface elevation plots of: (a) ocean swell produced using the EY spectrum in Figure 4(a), (b) ocean swell travelling against a surface current produced using the EY spectrum and current influence spectrum in Figure 4(b). Both plots are comprised of 512^2 waves.

of the TMA spectrum decreases with reducing water depth, i.e. the waves have less energy. For deep water, $d \to \infty$, the TMA spectrum converges to the JONSWAP spectrum. The unidirectional TMA spectrum is [17]:

$$S_{\text{TMA}}(k, \Lambda_{\text{TMA}}) = \frac{\alpha}{2} k^{-3} \phi_{\text{PM}}(\omega) \phi_{\text{J}}(\omega), \tag{10}$$

where parameter vector $\Lambda_{\text{TMA}} = \begin{bmatrix} \bar{U}_w & d & \bar{\beta}_w \end{bmatrix}^\top$, $\bar{U}_w$ is the mean local windspeed 10 metres above sea level, d is the water depth, $\bar{\beta}_w$ is the mean principle local wind direction,

$$\alpha = 0.0078 \kappa^{0.49}, \quad \kappa = \frac{\bar{U}_w^2 k_p}{g}, \quad \phi_{\text{PM}}(\omega) = \exp\left(-\frac{5}{4}\left\{\frac{\omega}{\omega_p}\right\}^{-4}\right), \quad \omega_p = 0.2\pi,$$

$$\phi_{\text{J}}(\omega) = \exp\left[\ln(\gamma) \exp\left(-(\omega - \omega_p)^2 / 2\sigma^2 \omega_p^2\right)\right], \quad \gamma = 3.3,$$

$$\sigma = \begin{cases} 0.07 & \omega \leq \omega_p \\ 0.09 & \omega > \omega_p \end{cases}.$$

The linear dispersion relation is used to numerically convert peak angular frequency, ω_p to peak wavenumber, k_p, i.e.:

$$\omega_p^2 = g k_p \tanh(k_p d).$$

The finite water depth effects are produced via this relation.

In order to compute the directional wave spectrum as in (5), a spreading function is required. The wave environment model uses the 'Cosine-2s' spreading function with the TMA unidirectional
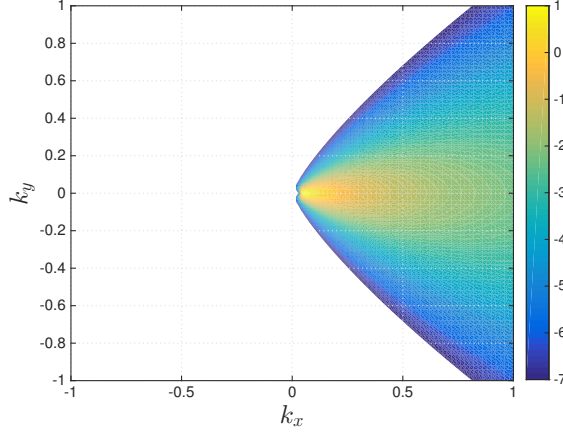
8

Figure 6: A contour plot of $\log_{10} \Psi_{\text{TMA}}(k_x = k\cos(\theta), k_y = k\sin(\theta))$ for Southerly mean local windspeed 10m/s, $s = 50$, $d = 20$m and corresponding to Sea State 3.

spectrum to model local wind effects, which is given as [24]:

$$D_{\text{TMA}}(\theta, \Lambda_{\text{TMA}}) = \left(\frac{2^{(2s-1)}}{\pi}\right)\left(\frac{\Gamma^2(s+1)}{\Gamma(2s+1)}\right)\cos^{2s}\left(\frac{\theta + \bar{\beta}_w}{2}\right), \qquad (11)$$

where s is called the spreading parameter and $\Gamma(\cdot)$ denotes the gamma function:

$$\Gamma(n) = (n-1)! \, . \qquad (12)$$

The larger the value of s, the more the waves are aligned with the principle wind direction. It makes physical sense that waves generated by local winds will be closely aligned with the wind direction, therefore a high spreading parameter of $s = 50$ is used. An example directional TMA spectrum is plotted in Figure 6. When compared to the EY spectrum plotted in Figure 4(a), the TMA spectrum is shown to be a lot less directional, with the majority of energy allotted to a narrow band of waves closely aligned with the principle wind direction. This can be seen more easily in the sea-surface plot shown in Figure 7 which was produced using the spectrum plotted in Figure 6.

3.3. Nwogu's current influence spectrum

Surface currents can be produced by various environmental forces such as tide, wind and the Coriolis effect. Currents of sufficient speed can have large effects on surface waves. When waves travel against a current, they increase in amplitude and may eventually break. Waves travelling with a current will reduce in amplitude. Nwogu [20] devised a method for altering a wave energy spectrum to include the effects of a surface current. This is achieved by element-wise multiplying a wave spectrum with no current, Ψ, with a current influence spectrum $C(k, \theta)$. The current influence spectrum is defined as [20]:

$$C(k, \theta, \Lambda_{\text{N}}) := \frac{kC_{g0}}{k_0(C_g + U_c\cos\theta)}\left[1 - \frac{U_c k\cos\theta}{\omega}\right], \qquad (13)$$
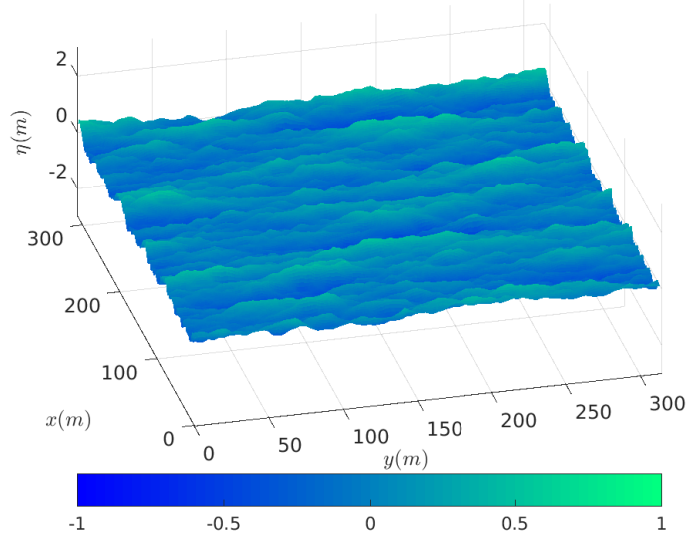
9

Figure 7: A sea-surface elevation plot of local wind-driven waves produced using the TMA spectrum plotted in Figure 6 comprised of 512^2 waves.

where parameter vector $\Lambda_{\mathrm{N}} = \begin{bmatrix} U_c & \beta_c \end{bmatrix}^\top$, U_c is the surface current speed, β_c is the principle current direction,

$$k_0 \cos \Delta\theta_{0,c} = k \cos \Delta\theta_c, \quad \Delta\theta_{0,c} = \beta_c - \theta_0, \quad \Delta\theta_c = \beta_c - \theta,$$

$C_g := \partial\omega/\partial k$ is the group velocity of the waves relative to the current and variables with subscript $_0$ denote values without the effects of current. The main limitation with the above model is that it produces unrealistically large values for the directional energy spectrum as $C_g + U_c \cos\theta$ approaches zero. Waves can no longer penetrate the current when the limit $C_g = -U_c \cos\theta$ is reached and in reality, would break before reaching that point. The wave environment model neither models nor simulates breaking waves. Therefore, Nwogu's current influence spectrum is modified in two ways. Firstly, the amplitude of "breaking waves" is set to zero, i.e. $C = 0$ if $C_g \leq -U_c \cos\theta$. Secondly, saturation limits are applied to the higher wavenumbers in the spectrum to prevent unphysical amplitudes of high spatial frequency waves. This is achieved by multiplying the current influence spectrum by k_0^{-5} for wavenumbers $k_0 > 1$. Figure 4(b) shows the effects of current on the EY spectrum shown in Figure 4(a). The current is travelling in the opposite direction to the principle swell wind direction. This has the effect of reducing the directionality of the spectrum and increasing the energy of the higher spatial frequency wave components. This is illustrated more clearly in the surface elevation plot shown in Figure 5(b) which was produced using the spectrum shown in Figure 4(b).

3.4. Variable environment implementation

Conditions at sea can change rapidly and it is therefore useful to simulate a USV's autonomy management system in time-varying wave environments. The wave environment model allows the following environmental factors to vary over time within a single simulation: swell windspeed U_s,

10

mean local windspeed $\bar{U}_w$, local wind principle direction β_w, surface current speed U_c, and surface current principle direction β_c. These environmental factors vary in the following manner.

For swell windspeed, EY spectra are generated for the initial swell windspeed at time $t = T_i$ and the final swell windspeed at time $t = T_f$. The implemented spectrum then changes linearly from the initial to the final spectra by means of a gradient matrix G_{EY}:

$$G_{\mathrm{EY}} = \frac{\Psi_{\mathrm{EY}}(k, \theta, \Lambda_{\mathrm{EY}}(T_f)) - \Psi_{\mathrm{EY}}(k, \theta, \Lambda_{\mathrm{EY}}(T_i))}{T_f - T_i},$$

$$\Psi_{\mathrm{EY}}(k, \theta, \Lambda_{\mathrm{EY}}(t)) = \begin{cases} \Psi_{\mathrm{EY}}(k, \theta, \Lambda_{\mathrm{EY}}(T_i)) & t \leq T_i \\ \Psi_{\mathrm{EY}}(k, \theta, \Lambda_{\mathrm{EY}}(T_i)) + G_{\mathrm{EY}}[t - T_i] & T_i \leq t \leq T_f \\ \Psi_{\mathrm{EY}}(k, \theta, \Lambda_{\mathrm{EY}}(T_f)) & t \geq T_f \end{cases}.$$

Similarly for mean local windspeed:

$$G_{\mathrm{TMA,S}} = \frac{S_{\mathrm{TMA}}(k, \Lambda_{\mathrm{TMA}}(T_f)) - S_{\mathrm{TMA}}(k, \Lambda_{\mathrm{TMA}}(T_i))}{T_f - T_i},$$

$$S_{\mathrm{TMA}}(k, \Lambda_{\mathrm{TMA}}(t)) = \begin{cases} S_{\mathrm{TMA}}(k, \Lambda_{\mathrm{TMA}}(T_i)) & t \leq T_i \\ S_{\mathrm{TMA}}(k, \Lambda_{\mathrm{TMA}}(T_i)) + G_{\mathrm{TMA,S}}[t - T_i] & T_i \leq t \leq T_f \\ S_{\mathrm{TMA}}(k, \Lambda_{\mathrm{TMA}}(T_f)) & t \geq T_f \end{cases},$$

and local wind principle direction.

$$G_{\mathrm{TMA,D}} = \frac{D_{\mathrm{TMA}}(\theta, \Lambda_{\mathrm{TMA}}(T_f)) - D_{\mathrm{TMA}}(\theta, \Lambda_{\mathrm{TMA}}(T_i))}{T_f - T_i},$$

$$D_{\mathrm{TMA}}(\theta, \Lambda_{\mathrm{TMA}}(t)) = \begin{cases} D_{\mathrm{TMA}}(\theta, \Lambda_{\mathrm{TMA}}(T_i)) & t \leq T_i \\ D_{\mathrm{TMA}}(\theta, \Lambda_{\mathrm{TMA}}(T_i)) + G_{\mathrm{TMA,D}}[t - T_i] & T_i \leq t \leq T_f \\ D_{\mathrm{TMA}}(\theta, \Lambda_{\mathrm{TMA}}(T_f)) & t \geq T_f \end{cases}.$$

The current influence spectrum is recalculated every time step of the simulation with linearly varying current speed and current direction:

$$G_{\mathrm{C,U}} = \frac{U_c(T_f) - U_c(T_i)}{T_f - T_i}, \quad G_{\mathrm{C},\beta} = \frac{\beta_c(T_f) - \beta_c(T_i)}{T_f - T_i},$$

$$U_c(t) = \begin{cases} U_c(T_i) & t \leq T_i \\ U_c(T_i) + G_{\mathrm{C,U}}[t - T_i] & T_i \leq t \leq T_f \\ U_c(T_f) & t \geq T_f \end{cases},$$

$$\beta_c(t) = \begin{cases} \beta_c(T_i) & t \leq T_i \\ \beta_c(T_i) + G_{\mathrm{C},\beta}[t - T_i] & T_i \leq t \leq T_f \\ \beta_c(T_f) & t \geq T_f \end{cases}.$$

11

3.5. Wind gust modelling

The wave environment model generates a gusting local wind in order to simulate realistic wind-induced forces, τ_{wind}, on the vessel. The local windspeed U_w is decomposed in the following manner:

$$U_w(t) = \bar{U}_w + \lambda_g U_g(t), \tag{14}$$

where $\bar{U}_w$ is the mean windspeed 10 metres above sea level, U_g is the gust component and λ_g is a gust factor. In a similar fashion to surface waves, several spectral models have been developed for wind gusts. The NPD wind gust spectrum is used which has the form [25]:

$$S_{\text{NPD}}(f) = 320 \frac{\left(\frac{\bar{U}_w}{10}\right)^2}{(1 + x^n)^{\frac{5}{3n}}}, \quad x = 172 f \left(\frac{\bar{U}_w}{10}\right)^{-\frac{3}{4}}, \tag{15}$$

where $n=0.468$ and f is frequency in Hertz. The time-varying wind gust component is then calculated from:

$$U_g(t) = \sum_{i=1}^{N_f} \left[\sqrt{2 S_{\text{NPD}}(f_{\text{i}}) \Delta f} \cos\left(2\pi f_{\text{i}} t + \phi_{\text{i}}\right) \right], \tag{16}$$

where $\Delta f = |f_{\text{i+1}} - f_{\text{i}}|$ is the sample frequency interval, and $\phi \in [0, 2\pi]$ is random added phase. The wind gust factor λ_g in (14) can be varied to intensify or attenuate the strength of the gust component. An example plot of the gusting local wind variation is shown in Figure 8(a).

The local wind direction angle, β_w, also varies with time. Like for the local windspeed, the wind angle can also be decomposed into a mean component and varying component, i.e. $\beta_w = \bar{\beta}_w + \beta'_w$. The varying component is modelled using a 1st-order Gauss-Markov process [26]:

$$\dot{\beta}'_w + \mu \beta'_w = w, \tag{17}$$

where $\mu > 0$ is a constant fluctuation coefficient and w is white noise. Figure 8(b) shows an example plot of the wind angle variation.

The wind-induced forces experienced by a USV are modelled as [14]:

$$\tau_{\text{wind}} = \frac{1}{2} \rho_{\text{a}} V_{rw}^2 \begin{bmatrix} C_X(\gamma_{rw}) A_{Fw} \\ C_Y(\gamma_{rw}) A_{Lw} \\ 0 \\ C_K(\gamma_{rw}) A_{Lw} H_{Lw} \\ 0 \\ C_N(\gamma_{rw}) A_{Lw} L_{oa} \end{bmatrix}, \tag{18}$$

where $\rho_{\text{a}} = 1.225$ kg/m^3 is the density of air, A_{Fw} is the frontal exposed projected area of the vessel, A_{Lw} is the lateral exposed projected area of the vessel, H_{Lw} is the vertical coordinate above the waterline of the centroid of A_{Lw} and L_{oa} is the overall length of the vessel. The relative windspeed and angle are defined respectively:

$$V_{rw} = \sqrt{u_{rw}^2 + v_{rw}^2}, \tag{19a}$$
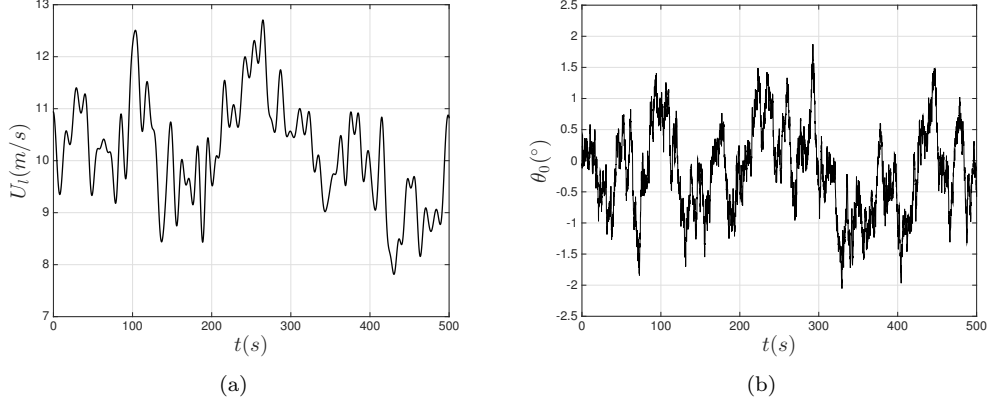
$$\gamma_{rw} = -\text{atan2}(v_{rw}, u_{rw}), \tag{19b}$$

12

Figure 8: (a) An example local windspeed variation with gusting component calculated from the NPD wind gust spectrum, for $\bar{U}_w = 10$m/s, $\lambda_g = 1$ and $N_f = 100$. (b) An example local wind angle variation, with fluctuations to the mean calculated using a 1$^{\text{st}}$-order Gauss-Markov process, for $\mu = 0.1$ and $\bar{\beta}_w = 0$.

where

$$u_{rw} = u - u_w, \quad v_{rw} = v - v_w,$$

$$u_w = U_w \cos(\beta_w - \psi), \quad v_w = U_w \sin(\beta_w - \psi),$$

u and v are the surge and sway velocities, and ψ denotes the heading angle of the vessel. The atan2 operator is defined as:

$$\text{atan2}(v, u) = \begin{cases} \arctan(\frac{v}{u}) & \text{if } u > 0, \\ \frac{\pi}{2} - \arctan(\frac{u}{v}) & \text{if } v > 0, \\ -\frac{\pi}{2} - \arctan(\frac{u}{v}) & \text{if } v < 0, \\ \arctan(\frac{v}{u}) \pm \pi & \text{if } x < 0, \\ \text{undefined} & \text{if } u = 0 \text{ and } v = 0. \end{cases} \tag{20}$$

Returning back to (18), $C_X(\gamma_{rw})$, $C_Y(\gamma_{rw})$, $C_K(\gamma_{rw})$ and $C_N(\gamma_{rw})$ denote wind drag coefficients in the surge, sway, roll and yaw degrees of freedom respectively. These coefficients vary with relative wind angle and can be obtained for a specific vessel from scale model testing or via a computational fluid dynamics program. For the current simulation model, the wind coefficients of Blendermann [27] are used. Blendermann performed wind tunnel tests on 17 different types of vessel and derived the following semi-empirical expressions for the coefficients:

$$C_X(\gamma_{rw}) = -CD_{l_{AF}}(\gamma_{rw}) \frac{\cos(\gamma_{rw})}{1 - \frac{\delta}{2}\left(1 - \frac{CD_l}{CD_t}\right)\sin^2(2\gamma_{rw})}, \tag{21a}$$

$$C_Y(\gamma_{rw}) = CD_t \frac{\sin(\gamma_{rw})}{1 - \frac{\delta}{2}\left(1 - \frac{CD_l}{CD_t}\right)\sin^2(2\gamma_{rw})}, \tag{21b}$$

13

Parameter	Symbol	Value
Lateral resistance coeff.	CD_t	0.90
Longitudinal resistance coeff. (head wind)	$CD_{l_{AF}}(\gamma_{rw} <= \pi/2)$	0.55
Longitudinal resistance coeff. (tail wind)	$CD_{l_{AF}}(\gamma_{rw} > \pi/2)$	0.60
Cross-force parameter	δ	0.60
Rolling moment factor	κ	1.1
Frontal projected area	A_{Fw}	2.4m^2
Lateral projected area	A_{Lw}	16m^2
Horizontal coordinate of centroid of A_{Lw}	s_L	-1.2m
Vertical coordinate of centroid of A_{Lw}	H_{Lw}	0.7m

Table 2: Wind-induced force parameters for Halcyon. Parameters 1-5 taken from Blendermann [27] for vessel type: 'Speed boat'.

$$C_K(\gamma_{rw}) = \kappa C_Y(\gamma_{rw}), \tag{21c}$$

$$C_N(\gamma_{rw}) = \left[\frac{s_L}{L_{oa}} - 0.18 \left(\gamma_{rw} - \frac{\pi}{2} \right) \right] C_Y(\gamma_{rw}), \tag{21d}$$

where $CD_{l_{AF}}$ is the longitudinal resistance coefficient, CD_t is the lateral resistance coefficient, δ is the cross-force parameter, κ is the rolling moment factor, $CD_l = CD_{l_{AF}}(\gamma_{rw}) \frac{A_{Fw}}{A_{Lw}}$ and s_L is the horizontal coordinate of the centroid of the transverse projected area A_{Lw} with respect to the main section. The coefficients used for Halcyon are summarised in Table 2.

4. Reference frames

In order to model the rigid body motions of a craft, a number of reference frames must be defined. In modelling Halcyon, two reference frames are used: a body-fixed reference frame which shall be referred to as the b-frame, and a North-East-Down (NED) reference frame which shall be referred to as the n-frame.

The b-frame is fixed to and moves with the vessel and has its origin, O_b, at some fixed location on the vessel. In what follows, this origin is set at the location of Halcyon's centre of gravity. The co-ordinate system used in the b-frame is illustrated in Figure 9 where it can be seen that x_b lies in the horizontal plane and points from aft to fore, y_b lies in the horizontal plane and points from port to starboard, and z_b lies in the vertical plane and points downwards. The vessel's linear and angular velocities are expressed in this reference frame.

The n-frame is fixed to and moves with the earth and has it's origin, O_n, at a prescribed location on the earth's surface. It is defined as a tangent plane on the earth's surface centred at O_n and is therefore only applicable for vessels operating in an area close to this origin; otherwise knows as flat earth navigation. The n-frame shall be considered inertial. The co-ordinate system used is illustrated in Figure 9. Axis x_n points towards true North, axis y_n points towards East, and axis z_n points down towards the centre of the Earth. Linear and angular positions are expressed in this reference frame.

SNAME notation [28] is used in the following to denote motions and rotations in all six degrees of freedom. This is summarised in Table 3. Angles are defined using the right-hand rule.
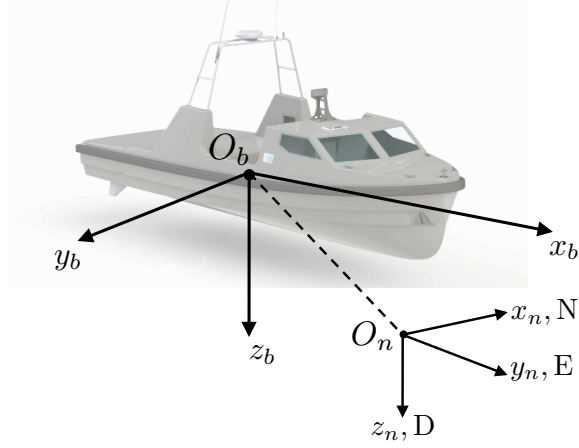
14

Figure 9: A diagram illustrating the body-fixed reference frame with origin O_b and the North-East-Down (NED) reference frame with origin O_n.

DOF	Description	Forces/ moments	Linear/ angular velocities	Position/ Euler angles
1	Linear motion along x (Surge)	X	u	x_n
2	Linear motion along y (Sway)	Y	v	y_n
3	Linear motion along z (Heave)	Z	w	z_n
4	Angular motion about x (Roll)	K	p	ϕ
5	Angular motion about y (Pitch)	M	q	θ
6	Angular motion about z (Yaw)	N	r	ψ

Table 3: SNAME notation [28] for a vessel.

5. 6 DOF rigid body boat dynamics

There are two distinct frameworks which can be followed for modelling marine craft: Manoeuvring Theory and Seakeeping Theory. Manoeuvring Theory assumes that a ship is moving in calm waters such that hydrodynamic coefficients are frequency independent. This results in a ship only having significant dynamics in surge, sway and yaw (degrees of freedom in the horizontal plane) [14]. Manoeuvring models can be either linear or nonlinear. Seakeeping theory models are usually derived in a linear framework and they include frequency-dependent hydrodynamic coefficients and wave-induced forces. Hydrodynamic numerical programs are required to generate the frequency-dependent model parameters based on hull geometry and mass distribution. Seakeeping models are therefore better able to capture a boat's dynamics in rougher seas.

A Seakeeping-type model is required to accurately simulate Halcyon, owing to the need to gain accurate data for the orientation and angular velocities of the boat; especially in higher sea states. Therefore, the Nonlinear Unified Seakeeping and Manoeuvring Model with Fluid Memory Effects is used. This is primarily a linear Seakeeping model with nonlinear damping and Coriolis-centripetal forces included and is given as [12]:

$$\dot{\boldsymbol{\eta}} = \boldsymbol{J}_\Theta(\boldsymbol{\eta})\boldsymbol{\nu}, \tag{22a}$$

$$\boldsymbol{M}\dot{\boldsymbol{\nu}} + \boldsymbol{C}_{RB}(\boldsymbol{\nu})\boldsymbol{\nu} + \boldsymbol{C}_A(\boldsymbol{\nu_r})\boldsymbol{\nu_r} + \boldsymbol{D}(\boldsymbol{\nu_r})\boldsymbol{\nu_r} + \boldsymbol{\mu} + \boldsymbol{G}\boldsymbol{\eta} = \boldsymbol{\tau}_{\text{wind}} + \boldsymbol{\tau}_{\text{wave}} + \boldsymbol{\tau}, \tag{22b}$$

where:

$\boldsymbol{\eta} := [x_n, y_n, z_n, \phi, \theta, \psi]^\top$ is a vector of position and Euler angles in the n-frame,

$\boldsymbol{\nu} := [u, v, w, p, q, r]^\top$ is a vector of linear and angular velocities in the b-frame,

$\boldsymbol{\nu_r} := \boldsymbol{\nu} - \boldsymbol{\nu}_c \in \mathbb{R}^6$ is a vector of relative velocities where $\boldsymbol{\nu}_c$ is the ocean current velocity vector in the b-frame,

$\boldsymbol{M} := \boldsymbol{M}_{RB} + \boldsymbol{M}_A \in \mathbb{R}^{6\times 6}$ = rigid-body mass + hydrodynamic added mass matrices,

$\boldsymbol{C}_{RB}(\boldsymbol{\nu}) \in \mathbb{R}^{6\times 6}$ is a rigid-body Coriolis-centripetal matrix,

$\boldsymbol{C}_A(\boldsymbol{\nu}_r) \in \mathbb{R}^{6\times 6}$ is a hydrodynamic added mass Coriolis-centripetal matrix,

$\boldsymbol{D}(\boldsymbol{\nu}_r) := \boldsymbol{D} + \boldsymbol{D}_n(\boldsymbol{\nu}_r) \in \mathbb{R}^{6\times 6}$ = linear + nonlinear damping matrices,

$\boldsymbol{\mu} \in \mathbb{R}^6$ models fluid memory effects,

$\boldsymbol{G} \in \mathbb{R}^{6\times 6}$ models restoring forces, i.e. the effects of gravity and buoyancy,

$\boldsymbol{\tau}_{\textbf{wind}} \in \mathbb{R}^6$ is a vector of wind-induced forces,

$\boldsymbol{\tau}_{\textbf{wave}} \in \mathbb{R}^6$ is a vector of wave-induced forces,

$\boldsymbol{\tau} \in \mathbb{R}^6$ is a vector of control actuation forces, i.e. rudder and thrust,

and $\boldsymbol{J}_\Theta(\boldsymbol{\eta}) \in \mathbb{R}^{6\times 6}$ is an Euler angle transformation matrix between the b-frame and n-frame, defined as:

$$\boldsymbol{J}_\Theta(\boldsymbol{\eta}) = \left[\begin{array}{cc} \boldsymbol{R}_b^n(\boldsymbol{\eta}) & \boldsymbol{0}_{3\times 3} \\ \boldsymbol{0}_{3\times 3} & \boldsymbol{T}_\Theta(\boldsymbol{\eta}) \end{array} \right], \tag{23}$$

where,

$$\boldsymbol{R}_b^n(\boldsymbol{\eta}) = \begin{bmatrix} c(\psi)c(\theta) & -s(\psi)c(\phi) + c(\psi)s(\theta)s(\psi) & s(\psi)s(\phi) + c(\psi)c(\phi)s(\theta) \\ s(\psi)c(\theta) & c(\psi)c(\phi) + s(\phi)s(\theta)s(\psi) & -c(\psi)s(\phi) + s(\theta)s(\psi)c(\phi) \\ -s(\theta) & c(\theta)s(\phi) & c(\theta)c(\phi) \end{bmatrix},$$

$$\boldsymbol{T}_\Theta(\boldsymbol{\eta}) = \begin{bmatrix} 1 & s(\phi)t(\theta) & c(\phi)t(\theta) \\ 0 & c(\phi) & -s(\phi) \\ 0 & s(\phi)/c(\theta) & c(\phi)/c(\theta) \end{bmatrix},$$

and c, s and t denotes cosine, sine and tangent trigonometric functions respectively. All known rigid body model parameters for this section are summarised in Table 4.

The unified ship dynamics model in (22) includes nonlinear manoeuvring dynamics (e.g. Coriolis-centripetal and damping forces) and linear seakeeping dynamics (e.g. fluid memory effects, restoring forces, damping forces and wave-induced forces). The linear seakeeping dynamics are derived initially using a seakeeping reference frame (the s-frame) which is not fixed to a vessel like the b-frame but is instead fixed to the equilibrium state of a vessel. It is assumed that the s-frame moves at a constant speed, heading and orientation and is therefore considered inertial. By linearising velocities and displacements about the s-frame, the governing hydrodynamics are derived under the assumption that perturbations from the equilibrium state are small. It is for this reason that the model may lose accuracy when excited by large environmental disturbances.

5.1. Rigid-body mass matrix: $\boldsymbol{M}_{RB}$

The rigid-body mass matrix is defined as:

$$\boldsymbol{M}_{RB} := \begin{bmatrix} m\boldsymbol{I}_{3\times 3} & -m\boldsymbol{S}(\boldsymbol{r}_g^b) \\ m\boldsymbol{S}(\boldsymbol{r}_g^b) & \boldsymbol{I}_b \end{bmatrix} \tag{24}$$

where m is the mass of the boat, $\boldsymbol{I}_{3\times 3}$ is an identity matrix, $\boldsymbol{r}_g^b \in \mathbb{R}^3$ is a displacement vector between O_b and centre of gravity CG ($\boldsymbol{r}_g^b = 0$ in this case as $O_b = CG$), $\boldsymbol{I}_b$ is a moments of inertia matrix about O_b, and the cross-product operator is defined:

$$\boldsymbol{S}(\boldsymbol{\lambda}) = -\boldsymbol{S}^\top(\boldsymbol{\lambda}) = \begin{bmatrix} 0 & -\lambda_3 & \lambda_2 \\ \lambda_3 & 0 & -\lambda_1 \\ -\lambda_2 & \lambda_1 & 0 \end{bmatrix}, \quad \boldsymbol{\lambda} = \begin{bmatrix} \lambda_1 \\ \lambda_2 \\ \lambda_3 \end{bmatrix}. \tag{25}$$

5.2. Added mass matrix: $\boldsymbol{M}_A$

A marine craft which is not at rest relative to the sea-surface will induce motion in the surrounding water. The kinetic energy required for the craft's hull to move the surrounding water is accounted for by adding a hydrodynamic virtual mass to the vessel. The added mass matrix is defined as: $\boldsymbol{M}_A(U) := \boldsymbol{A}(\omega = \infty, U)$, where $\boldsymbol{A}(\omega, U)$ are the hydrodynamic added mass potential coefficient matrices specific to Halcyon which vary with angular frequency ω and forward speed U. All of Halcyon's hydrodynamic parameters have been computed using the University of Southampton's hydrodynamic program THARBM [4].

17

5.3. Coriolis-centripetal matrices: $\boldsymbol{C}_{RB}(\boldsymbol{\nu})$ and $\boldsymbol{C}_A(\boldsymbol{\nu_r})$

The nonlinear Coriolis-centripetal matrices are defined as:

$$\boldsymbol{C}(\boldsymbol{\nu}) := \left[\begin{array}{cc} 0 & -\boldsymbol{S}(\boldsymbol{M}_{11}\boldsymbol{\nu}_1 + \boldsymbol{M}_{12}\boldsymbol{\nu}_2) \\ -\boldsymbol{S}(\boldsymbol{M}_{11}\boldsymbol{\nu}_1 + \boldsymbol{M}_{12}\boldsymbol{\nu}_2) & -\boldsymbol{S}(\boldsymbol{M}_{21}\boldsymbol{\nu}_1 + \boldsymbol{M}_{22}\boldsymbol{\nu}_2) \end{array} \right]. \tag{26}$$

For the rigid body Coriolis-centripetal matrix $\boldsymbol{C}_{RB}(\boldsymbol{\nu})$:

$$\boldsymbol{M}_{RB} = \left[\begin{array}{cc} \boldsymbol{M}_{11} & \boldsymbol{M}_{12} \\ \boldsymbol{M}_{21} & \boldsymbol{M}_{22} \end{array} \right], \quad \boldsymbol{\nu} = \left[\begin{array}{c} \boldsymbol{\nu}_1 \\ \boldsymbol{\nu}_2 \end{array} \right],$$

and for the added mass Coriolis-centripetal matrix $\boldsymbol{C}_A(\boldsymbol{\nu_r})$:

$$\boldsymbol{M}_A = \left[\begin{array}{cc} \boldsymbol{M}_{11} & \boldsymbol{M}_{12} \\ \boldsymbol{M}_{21} & \boldsymbol{M}_{22} \end{array} \right], \quad \boldsymbol{\nu_r} = \left[\begin{array}{c} \boldsymbol{\nu}_1 \\ \boldsymbol{\nu}_2 \end{array} \right].$$

5.4. Restoring forces matrix: $\boldsymbol{G}$

The linear restoring forces matrix is defined as:

$$\boldsymbol{G} := \left[\begin{array}{cccccc} 0 & 0 & 0 & 0 & 0 & 0 \\ 0 & 0 & 0 & 0 & 0 & 0 \\ 0 & 0 & G_{33} & 0 & G_{35} & 0 \\ 0 & 0 & 0 & G_{44} & 0 & 0 \\ 0 & 0 & G_{53} & 0 & G_{55} & 0 \\ 0 & 0 & 0 & 0 & 0 & 0 \end{array} \right], \tag{27}$$

where,

$$G_{33} = \rho_{\mathrm{w}} g A_{wp}, \quad G_{44} = \rho_{\mathrm{w}} g \overline{GM_T} \nabla, \quad G_{55} = \rho_{\mathrm{w}} g \overline{GM_L} \nabla,$$

$$G_{35} = G_{53} = \rho_{\mathrm{w}} g A_{wp} (L_{CG} - L_{CF}),$$

A_{wp} is the water plane area at equilibrium, ∇ is the nominal displaced water volume, $\overline{GM_T}$ is the transverse metacentric height, $\overline{GM_L}$ is the longitudinal metacentric height, and L_{CG} and L_{CF} are the longitudinal distances to the vessel's centre of gravity and centre of flotation respectively.

5.5. Fluid memory effects: $\boldsymbol{\mu}$

A moving vessel will generate waves on the sea-surface which will theoretically persist at all future times. These waves will potentially have a dampening effect on all of the vessel's degrees of freedom. These time-dependent damping forces are known as 'fluid memory effects' [29]. These can be modelled as:

$$\boldsymbol{\mu} := \int_0^t \boldsymbol{K}(t - \tau) \underbrace{[\boldsymbol{\nu}_r(\tau) - U\boldsymbol{e}_1]}_{\delta\boldsymbol{\nu}_r} \, d\tau, \tag{28}$$

where,

$$\boldsymbol{K}(t) = \frac{2}{\pi} \int_0^\infty [\boldsymbol{B}_{\mathrm{Total}}(\omega) - \boldsymbol{B}_{\mathrm{Total}}(\infty)] \cos(\omega t) \, d\omega, \quad \boldsymbol{B}_{\mathrm{Total}}(\omega) := \boldsymbol{B}(\omega, U = 0) + \boldsymbol{D}_V,$$

U denotes forward speed, $\boldsymbol{e}_1$ is a unit vector aligned with axis x_b, $\boldsymbol{K}(t)$ is a matrix of retardation functions, $\boldsymbol{B}(\omega, U)$ is a matrix of forward speed-dependent hydrodynamic potential damping coefficients and $\boldsymbol{D}_V$ is a viscous damping matrix.

Frequency-domain identification can be used to fit a transfer function to (28), such that $\boldsymbol{\mu} = \boldsymbol{H}(s)\delta\boldsymbol{\nu}_r$, where $\boldsymbol{H}(s) := \boldsymbol{C}_r(s\boldsymbol{I} - \boldsymbol{A}_r)^{-1}\boldsymbol{B}_r$, with corresponding time-domain state-space model [30]:

$$\dot{\boldsymbol{x}} = \boldsymbol{A}_r\boldsymbol{x} + \boldsymbol{B}_r\delta\boldsymbol{\nu}_r, \tag{29a}$$

$$\boldsymbol{\mu} = \boldsymbol{C}_r\boldsymbol{x}. \tag{29b}$$

The MSS FDI toolbox [31] was used to find the state-space models in (29). This frequency-domain identification method requires hydrodynamic matrices $\boldsymbol{A}(\omega, U)$ and $\boldsymbol{B}(\omega, U)$ which were computed using the hydrodynamic code THARBM [4].

5.6. Linear damping matrix: $\boldsymbol{D}$

The linear damping matrix is defined as:

$$\boldsymbol{D} := \boldsymbol{D}_P(U) + \boldsymbol{D}_V, \tag{30}$$

where: $\boldsymbol{D}_P(U) = \boldsymbol{B}(\omega = \infty, U)$ is a forward speed-dependent potential damping matrix of the form:

$$\boldsymbol{D}_P(U) := \begin{bmatrix} 0 & 0 & 0 & 0 & 0 & 0 \\ 0 & Y_v(U) & 0 & Y_p(U) & 0 & Y_r(U) \\ 0 & 0 & Z_w(U) & 0 & Z_q(U) & 0 \\ 0 & K_v(U) & 0 & K_p(U) & 0 & K_r(U) \\ 0 & 0 & M_w(U) & 0 & M_q(U) & 0 \\ 0 & N_v(U) & 0 & N_p(U) & 0 & N_r(U) \end{bmatrix}, \tag{31}$$

and $\boldsymbol{D}_V$ is a linear viscous damping matrix of the form:

$$\boldsymbol{D}_V = \text{diag}\left\{\boldsymbol{D}_{V_{11}}, \boldsymbol{D}_{V_{22}}, \boldsymbol{D}_{V_{33}}, \boldsymbol{D}_{V_{44}}, \boldsymbol{D}_{V_{55}}, \boldsymbol{D}_{V_{66}}\right\}. \tag{32}$$

The matrix entries in (32) can be computed using the following formulae [14]:

$$\boldsymbol{D}_{V_{11}} = \frac{m + A_{11}(0)}{T_{\text{surge}}}, \quad \boldsymbol{D}_{V_{22}} = \frac{m + A_{22}(0)}{T_{\text{sway}}},$$

$$\boldsymbol{D}_{V_{33}} = 2\Delta\zeta_{\text{heave}}\omega_{\text{heave}}\left[m + A_{33}(\omega_{\text{heave}})\right], \quad \boldsymbol{D}_{V_{44}} = 2\Delta\zeta_{\text{roll}}\omega_{\text{roll}}\left[I_{xx} + A_{44}(\omega_{\text{roll}})\right],$$

$$\boldsymbol{D}_{V_{55}} = 2\Delta\zeta_{\text{pitch}}\omega_{\text{pitch}}\left[I_{yy} + A_{55}(\omega_{\text{pitch}})\right], \quad \boldsymbol{D}_{V_{66}} = \frac{I_{zz} + A_{66}(0)}{T_{\text{yaw}}},$$

where $\Delta\zeta_-$ denotes additional damping parameters, ω_- are resonant frequencies, T_- denotes time constants and A_{ij} identifies terms within the hydrodynamic added mass matrix. However, Halcyon's resonant frequencies and time constants are unknown a priori. Therefore, these parameters were identified from the sea-trials data. This will be discussed further in Section 8.

5.7. Nonlinear damping: $\boldsymbol{D}_n(\boldsymbol{\nu}_r)$

The nonlinear damping forces only have components in surge (u, X), sway (v, Y) and yaw (ψ, N), such that:

$$\boldsymbol{D}_n(\boldsymbol{\nu}_r) = \begin{bmatrix} X_{D_n}(\boldsymbol{\nu}_r) & Y_{D_n}(\boldsymbol{\nu}_r) & 0 & 0 & 0 & N_{D_n}(\boldsymbol{\nu}_r) \end{bmatrix}^{\top}. \tag{33}$$

19

5.7.1. Nonlinear surge resistance

The surge resistance force X_{D_n}, aligned with the x-axis of the boat's reference frame, can be defined as [32]:

$$X_{D_n}(\boldsymbol{\nu}_r) = -\frac{1}{2}\rho_{\mathrm{w}}SC_f^*(u_r)|u_r|u_r, \tag{34}$$

where,

$$C_f^*(u_r) = C_f(u^{\mathrm{max}}) + \left(\frac{A_x}{S}C_x - C_f(u^{\mathrm{max}})\right)\exp(-\alpha u_r^2),$$

$$C_f(u_r) = \frac{0.075}{(\log_{10}Re - 2)^2} + C_R, \quad Re := \frac{u_r L_{pp}}{\nu},$$

S is the wetted surface area of the hull (assumed constant), u_r is the relative surge velocity component of $\boldsymbol{v_r}$, u^{max} is the maximum forward speed of the vessel, A_x is the frontal projected area of the boat below the waterline, Re denotes Reynolds number, $\nu = 1 \times 10^{-6}\mathrm{m/s^2}$ is the kinematic viscosity of salt water, $C_f(u_r)$ is the resistance curve, $C_f^*(u_r)$ is the modified resistance curve which ensures higher resistance coefficients at low forward speeds, C_R denotes residual resistance, C_x is the current coefficient, and $\alpha > 0$ is a constant. Parameters C_R, C_x and α are unknown for Halcyon a priori and are determined using sea-trials data. This will be discussed more in Section 8.

5.7.2. Nonlinear sway and yaw resistance

The nonlinear damping forces in sway, Y_{D_n}, and yaw, N_{D_n}, can be computed using the cross-flow drag principle as [33]:

$$Y_{D_n}(\boldsymbol{\nu}_r) = -\frac{1}{2}\rho_{\mathrm{w}}TC_d^{2D}\int_{-L_{pp}/2}^{L_{pp}/2}|v_r + xr|(v_r + xr)\,dx, \tag{35a}$$

$$N_{D_n}(\boldsymbol{\nu}_r) = -\frac{1}{2}\rho_{\mathrm{w}}TC_d^{2D}\int_{-L_{pp}/2}^{L_{pp}/2}x|v_r + xr|(v_r + xr)\,dx, \tag{35b}$$

where T is the vessel's draft, v_r is the relative sway velocity component of $\boldsymbol{v_r}$ and r is the yaw rate. The two-dimensional cross-flow drag coefficient, C_d^{2D}, is approximated using Hoerner's curve [34] which gives a value based on a vessel's beam length and draft.

6. Actuation dynamics

The vector of actuation forces, $\tau \in \mathbb{R}^6$, is a summation of the rudder forces and propulsion forces, i.e.:

$$\tau(t) = \tau_{\mathrm{rudder}}(t) + \tau_{\mathrm{prop}}(t).$$

A rudder dynamics model and a propeller-engine dynamics model are used to simulate τ_{rudder} and τ_{prop} respectively. These will be outlined in the following sections.

Description	Symbol	Value	Units
Total mass	m	11000	kg
Roll moment of inertia about CoG	I_{xx}	6982	$\text{kg} \cdot \text{m}^2$
Pitch moment of inertia about CoG	I_{yy}	39077	$\text{kg} \cdot \text{m}^2$
Yaw moment of inertia about CoG	I_{zz}	36062	$\text{kg} \cdot \text{m}^2$
Length between perpendiculars	L_{pp}	11.2	m
Beam	B	3.2	m
Draft	T	0.7	m
Wetted hull surface area	S	36.4	m^2
Displaced water volume	∇	10.7	m^3
Water plane area at equilibrium	A_{wp}	27.4	m^2
Frontal projected area above waterline	A_{fw}	2.4	m^2
Lateral projected area above waterline	A_{lw}	16.5	m^2
Transverse metacentric height	$\overline{GM_T}$	1.7	m
Longitudinal metacentric height	$\overline{GM_L}$	20.6	m
Frontal projected area below waterline	A_x	2.1	m^2
Two-dimensional cross-flow drag coefficient	C_D^{2D}	0.63	–
Longitudinal distance between CG and CF	$L_{CG} - L_{CF}$	-0.37	m
Maximum forward speed of vessel	$u_{\max}$	12.8	m/s

Table 4: Halcyon's rigid body model parameters.

6.1. Rudder dynamics

A rudder moving through water is analogous to a wing moving through air and are therefore modelled similarly. Halcyon's two rudders produce non-zero forces/moments in surge (X_r), sway (Y_r), roll (K_r) and yaw (N_r) such that:

$$\tau_{\text{rudder}} = \begin{bmatrix} X_r & Y_r & 0 & K_r & 0 & N_r \end{bmatrix}^\top .$$

The surge force is due to the drag induced by the rudders. The sway force is due to the lift produced by the rudders which in turn produces moments in roll and yaw. These forces and moments are modelled as:

$$X_r = - \left[\frac{\left(\frac{\partial C_L}{\partial \alpha} \alpha_e \right)^2}{\pi \text{AR}} + C_{D0} \right] \frac{1}{2} \rho_{\text{w}} A_r \left(u_r^2 + v_r^2 \right), \tag{36a}$$

$$Y_r = \left(\frac{\partial C_L}{\partial \alpha} \alpha_e \right) \frac{1}{2} \rho_{\text{w}} A_r \left(u_r^2 + v_r^2 \right), \tag{36b}$$

$$K_r = -Y_r V_{CG}, \quad N_r = -Y_r L_{CG}, \quad \alpha_e = \alpha_r - \text{atan2}(v_r, |u_r|),$$

where $\frac{\partial C_L}{\partial \alpha}$ is the linear lift coefficient-angle of attack gradient, α_e is the effective angle of attack of the rudders, α_r is the actual rudder angle, AR is the rudder aspect ratio, C_{D0} is the zero-lift drag coefficient, A_r is the planform area of the rudders, and V_{CG} and L_{CG} are the vertical and longitudinal distances between the vessel's centre of gravity and rudders respectively. The first term in the brackets in (36a) models lift-induced drag [35]. Halcyon's rudders' linear lift coefficient-angle of attack gradient, $\frac{\partial C_L}{\partial \alpha}$, and the zero lift drag coefficient, C_{D0}, are unknown a priori. These parameters were identified from sea-trials data. This will be discussed more in Section 8. Known rudder parameters are summarised in Table 5.

Description	Symbol	Value
Aspect ratio	AR	0.19
Planform area	A_r	0.19 m^2
Vertical distance between rudders and CoG	V_{CG}	1m
Longitudinal distance between rudders and CoG	L_{CG}	-4.71m

Table 5: Halcyon's rudder parameters.

Description	Symbol	Value
Diameter	D	0.6m
Number of blades	Z	5
Pitch to diameter ratio	P/D	1.14
Blade area ratio	A_e/A_o	0.9
Engine-propeller shaft gear ratio	G_E	2.5
Engine idle RPM	E_{idle}	700 RPM

Table 6: Halcyon's propeller/engine parameters.

6.2. Propeller-engine dynamics

Halcyon's two propellers produce a force in surge and a pitching moment, such that:

$$\tau_{\text{prop}} = \begin{bmatrix} X_p & 0 & 0 & 0 & M_p & 0 \end{bmatrix}^\top,$$

where the induced pitching moment is defined as $M_p = X_p V_{CG}$. A single propeller would induce a rolling moment, however, because Halcyon's two propellers revolve in opposite directions, the resultant rolling moment is zero. The thrust produced by each individual propeller, $T_p = X_p/2$, is modelled using a polynomial thrust coefficient, K_T, in the following manner [36]:

$$T_p = K_T(J)\rho_{\text{w}} n_p |n_p| D^4, \tag{37}$$

where,

$$K_T(J) = K_T^{\{1\}} J^2 + K_T^{\{2\}} J + K_T^{\{3\}}, \quad J = \frac{V_a}{n_p D}, \quad V_a = |u_r|,$$

n_p is the number of propeller revolutions per second (positive clockwise, negative anti-clockwise), D is the propeller diameter, J is termed the advance coefficient, V_a is the advance speed and $K_T^{\{i\}}$ are thrust polynomial coefficients.

The thrust characteristics of Halcyon's propellers are unknown. The known propeller parameters are summarised in Table 6. A large amount of thrust coefficient data exists for Wageningen B-series marine propellers [36]. This data set consists of high-order polynomial thrust coefficients, $K_T(J)$, for propellers with different configurations of blade number (Z), blade area ratio (A_e/A_o) and pitch to diameter ratio (P/D). In order to obtain thrust characteristics for Halcyon's propellers, a high-order thrust coefficient polynomial for a Wageningen B-series propeller with equivalent parameters was found. A second-order polynomial approximation was then computed using a curve-fitting algorithm which yielded the thrust polynomial coefficients:

$$K_T^{\{1\}} = 0.0041, \quad K_T^{\{2\}} = -0.5002, \quad K_T^{\{3\}} = 0.6008.$$
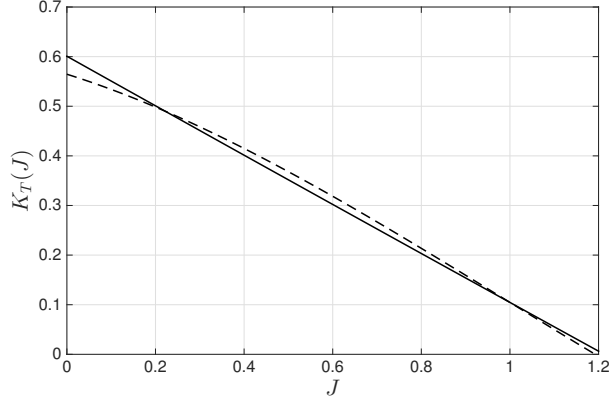
Figure 10: Thrust coefficient curves for a Wageningen B-series propeller with $Z = 5$, $P/D = 1.14$ and $A_e/A_o = 0.9$ (- -) and a second-order polynomial approximation (—).

Figure 10 compares the high-order polynomial thrust coefficient curve for the Wageningen B-series propeller with equivalent parameters and the second-order polynomial approximation.

The autonomy management system requires engine fuel consumption information for some of its control behaviours. Fuel consumption rate versus engine speed data is supplied with the engines. The engine speed is calculated from:

$$E_{RPM} = \begin{cases} G_E n_p & \text{if } G_E n_p > E_{\text{idle}} \\ E_{\text{idle}} & \text{otherwise} \end{cases}, \tag{38}$$

where G_E is the engine-propeller shaft gear ratio and E_{idle} is the engine idle speed.

7. Autopilot and the MOOS-IvP interface

The MOOS-IvP interface uses a Matlab wrapper called 'mex-moos' [37] to retrieve and send data to Halcyon's MOOS-IvP autonomy management system. Data sent from the simulation is numerous and includes GPS position, speed over ground and inertial measurement unit (IMU) data. The autonomy management system sends, via the MOOS-IvP interface, only a desired speed and a desired heading to the simulation. The autopilot then uses sensor data to determine a sufficient propeller speed and rudder position to ensure the vessel achieves these desired control objectives. The autopilot consists of a speed controller and a heading controller. Both incorporate proportional-integral-differential (PID) feedback controllers [38] in order to operate effectively.

7.1. Speed controller

A block diagram representation of the speed controller is shown in Figure 11. As can be seen from the figure, two PID controllers have been incorporated. The first (PID 1) takes in the error between the desired speed from the MOOS-IvP interface and the actual speed measured using a sensor, and outputs a desired thrust. The second PID controller (PID2) takes in the error between the desired thrust and the estimated actual thrust, and outputs a propeller shaft speed, n_p, which
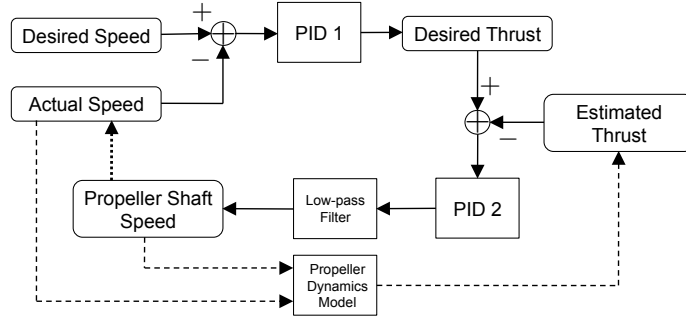
Figure 11: Block diagram representation of the autopilot's speed controller.
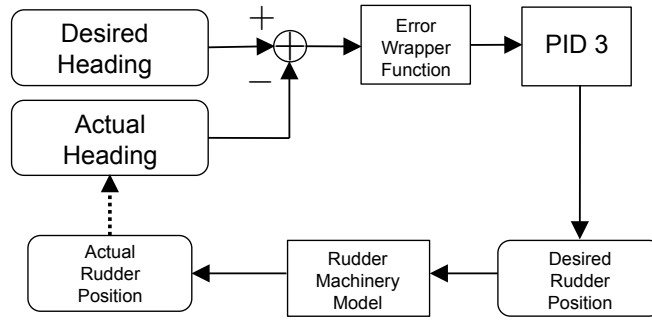

Figure 12: Block diagram representation of the autopilot's heading controller.

has been low-pass filtered. The new propeller shaft speed will then affect the vessel's actual speed. The estimated thrust is determined using the propeller dynamics model presented in Section 6.2. As this is the model used in the simulation, the estimated thrust is equal to the actual simulated thrust produced by the propellers. However, this would not be the case for an actual vessel. The low-pass filter [38] effectively models the throttle-engine response, preventing unrealistically quick changes in propeller shaft speed and is represented as:

$$\frac{dn_p}{dt}(t) = -\frac{1}{\tau_p}n_p(t) + \frac{1}{\tau_p}\hat{n}_p(t), \tag{39}$$

where $\hat{n}_p$ is the unfiltered output of PID 2, τ_p is the time-constant and an initial condition $n_p(0) = 0$ is assumed. The speed controller parameters used are summarised in Table 7.

7.2. Heading controller

A block diagram representation of the heading controller is shown in Figure 12. Here only one PID controller (PID 3) has been implemented. The error between the desired heading from the MOOS-IvP interface and the actual measured heading is passed through an error wrapper function. This function ensures the vessel never needs to change its heading by more than 180 degrees and

PID controller number/Description	Symbol	Value
	K_P	4000
1	K_I	500
	K_D	1500
	K_P	1
2	K_I	50
	K_D	0
	K_P	1.5
3	K_I	0.1
	K_D	0.4
Propeller shaft time-constant	τ_p	10
Rudder machinery time-constant	τ_r	0.1
Maximum rudder rate	γ_r	$40°/\text{sec}$

Table 7: Speed and heading angle controller parameters.

manipulates the heading error in the following way:

$$
e_H = \begin{cases} \hat{e}_H & -180 \leq \hat{e}_H \leq 180 \\ \hat{e}_H - 360 & \hat{e}_H > 180 \\ \hat{e}_H + 360 & \hat{e}_H < -180 \end{cases}, \tag{40}
$$

where e_H is the output of the error wrapper function and $\hat{e}_H$ is the error between the desired and actual headings. The PID controller uses the updated error to determine a desired rudder angle. This is passed to a rudder machinery model which in turn dictates the actual rudder angle which will ultimately affect the actual heading angle. A van Amerongen rudder machinery model [39] is employed of the form:

$$
\dot{\alpha}_r(t) = \left[\frac{\alpha_d(t) - \alpha_r(t)}{\tau_r} \right], \tag{41}
$$

where α_r is the actual rudder angle, α_d is the desired rudder angle, τ_r is a time-constant and the initial condition $\alpha_r(0) = 0$ is assumed. Saturation functions are employed in order to enforce:

$$
-\gamma_r \leq \dot{\alpha}_r \leq \gamma_r, \tag{42a}
$$

$$
-\alpha_r^{\max} \leq \alpha_r \leq \alpha_r^{\max}, \tag{42b}
$$

where γ_r is the maximum rudder angle rate and $\alpha_r^{\max}$ is the maximum rudder deflection angle. The heading angle controller parameters used are summarised in Table 7.

8. Sea-trials validation

Halcyon undertook sea-trials near the Isle of Wight, U.K. between 2nd-3rd March 2016. The trials were carried out in Sea State 2-3 conditions; Sea State 2 describes a sea-surface with a significant wave height[1] of between 0.1-0.5 metres and Sea State 3 describes a sea-surface with a

---

[1]The significant wave height (h_s) is defined as the mean of the highest third of a set of waves. The height of a wave is defined as the vertical distance between its crest and trough.

Description	Symbol/Definition	Units
Linear accelerations in x_b, y_b, z_b	$\ddot{x}(t), \ddot{y}(t), \ddot{z}(t)$	m/s^2
Roll, pitch and yaw angles	$\phi(t), \theta(t), \psi(t)$	degrees
Speed over ground	$\text{SoG} = \sqrt{u^2 + v^2}$	m/s
Speed through water	$\text{StW} = \sqrt{u_r^2 + v_r^2}$	m/s
Magnetic heading angle	$\psi_h(t)$	degrees
Latitude and Longitude	$[l, \mu]$	degrees
Engine rotational speed	E_{RPM}	RPM
Rudder deflection angle	α_r	degrees

Table 8: Description of the data types collected during Halcyon's sea-trials.

significant wave height of between 0.5-1.25 metres. Two different types of test were carried out, namely:

- Constant speed and heading navigation into a head sea[2].

- Constant speed and constant radius turning circle manoeuvres.

The types of data collected during the sea-trials are summarised in Table 8. Based on the data collected, two comparative tests were devised in order to validate the simulation model. These were:

1. Constant speed and heading navigation into a head sea - to compare linear accelerations and angular displacements at non-zero forward speed as well as surge resistance.
2. Turning circle tests at constant speed and identical rudder angle or heading angle - to compare rudder deflection angles and GPS positions.

Certain parameters were used to tune the model to ensure that the simulation output from all testing matched that from the sea-trials as closely as possible. These tuning parameters were unknown a priori and are summarised as:

- Viscous damping matrix: D_V - see Section 5.6

- Surge resistance model parameters: α, C_R, C_x - see Section 5.7.1

- Rudder model parameters: $\frac{\partial C_L}{\partial \alpha}, C_{D0}$ - see Section 6.1

The results from both comparative tests will be outlined in the following sections.

8.1. Head sea validation

The constant speed and heading navigation into a head sea testing was conducted at four different forward speeds during the sea-trials: $\approx 2.5 m/s$, $\approx 4 m/s$, $\approx 5 m/s$ and $\approx 6 m/s$. As the precise sea conditions during the sea-trials are unknown, simulations were conducted for low Sea State 2: significant wave height $h_s = 0.1m$, and high Sea State 3: significant wave height $h_s = 1.25m$. The surface waves simulated were completely local wind-driven with no swell. This

---

[2]A head sea is when the principle direction of the waves is opposite to that of the vessel.

was to ensure the waves were near unidirectional and thus represented "worst-case" head seas. No surface currents were included in the simulations. All simulations were ran for 500 seconds which was long enough for time-averaged quantities to converge. Typically, simulations took around 3 minutes of wall clock time to complete on a desktop computer with a 8×3.3GHz Intel Xeon processor.

8.1.1. Viscous damping matrix tuning

Initially, the damping matrix in (32) was constructed using the formulae in Section 5.6 with estimates of the resonant frequencies and time constants of each degree of freedom of motion. Each entry of this matrix was then manually adjusted by comparing linear acceleration and angular displacement data from the head sea sea-trials and the simulations. For ease of comparison between comparative data sets, the standard deviations of the linear acceleration and angular displacement time histories were computed. Using a trial-and-error procedure, a linear viscous damping matrix was chosen that ensured that Sea State 2 simulated data was consistently less than the sea trials data, and that Sea State 3 simulated data was consistently greater than the sea trials data. The viscous damping matrix obtained using this method ensures that the simulated vessel's linear accelerations and angular displacements are bounded from below and from above the actual vessel's.

Figure 13 compares the standard deviations of linear acceleration data from the sea-trials and the $h_s = 0.1m$ and $h_s = 1.25m$ simulations. It is apparent from the plots that the sea-trials data lies in between the two sets of simulation data which is to be expected. As sea-trials data is unavailable for surge velocities greater than six metres per second, it is currently not possible to know whether the high-speed simulated data is valid. However, it is reasonable to assume that the forces imparted by the waves will increase as forward speed increases and therefore the linear accelerations of the vessel will increase also. This is precisely what is shown in the high speed simulation data.

Figure 14 compares the standard deviations of the angular displacement data from the sea-trials and the $h_s = 0.1m$ and $h_s = 1.25m$ simulations. Again, the sea-trials data lies between the low and high Sea State simulation data. It should be noted that for the head sea validation testing, the rudder angle was set to zero during all simulations. This was to ensure that the simulation autopilot did not have an effect on the yaw and roll angles. It is interesting to note that of the simulated data, only the magnitude of the pitching angle increases significantly with increasing surge velocity. Perhaps this is to be expected because the speed of a vessel is unlikely to significantly affect its rolling or yawing behaviour when navigating into a head sea.

The viscous damping matrix found using the tuning procedure outlined is given as:

$$D_V = 10^4 \times \text{diag} \{0, 0.22, 1.29, 2.11, 0, 4.21\}. \tag{43}$$

8.1.2. Surge resistance model tuning

The nonlinear surge resistance model is outlined in Section 5.7.1. In order to parameterise this model, the current coefficient (C_x), the residual resistance coefficients ($C_R(u_r)$) and resistance decay coefficient (α) need to be determined. A prediction of the residual resistance variation $C_R(u_r)$ was obtained using the WUMTIA Power Prediction Software Version 09.09.15.2. Using the Wolfson Unit Chine Craft method [40], the total resistance of the vessel was estimated. The predicted residual resistance was then found by subtracting the frictional resistance coefficient calculated using the ITTC 1957 friction formula:

$$C_f^{ITTC}(u_r) = \frac{0.075}{(\log_{10} Re - 2)^2}, \quad Re := \frac{u_r L_{pp}}{\nu}. \tag{44}$$
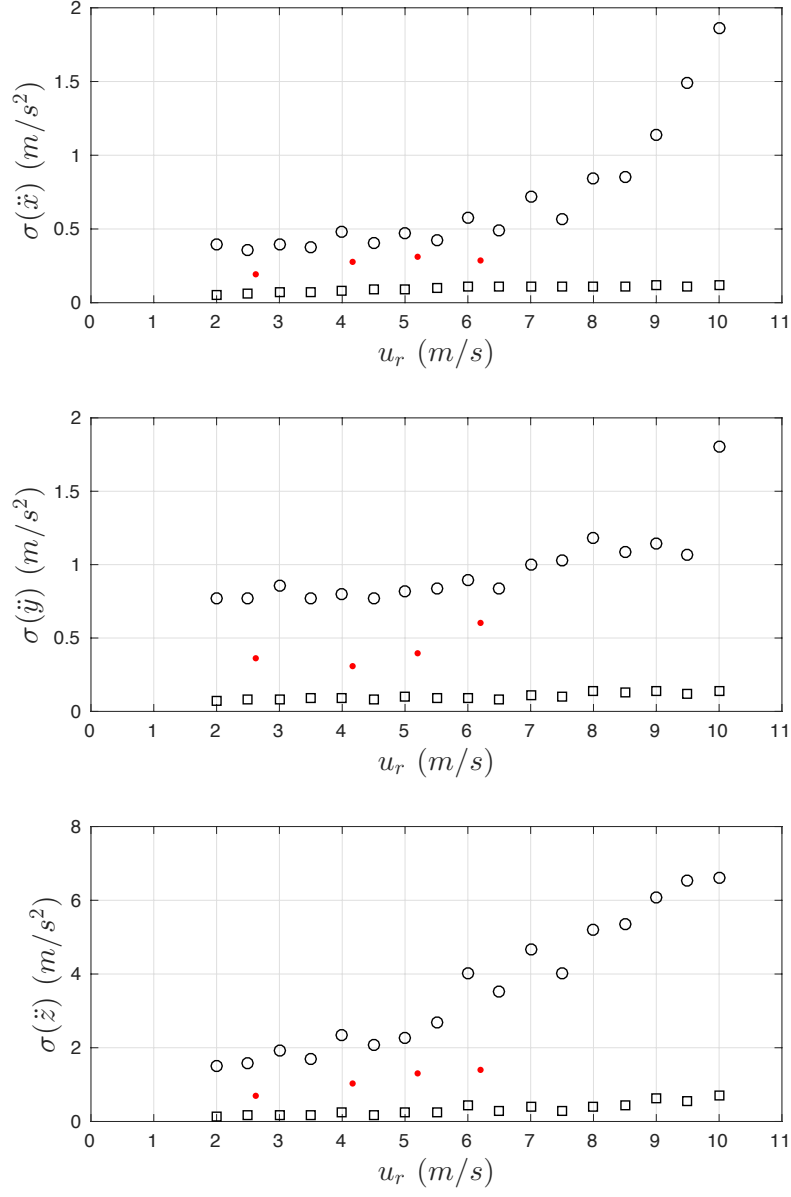
27

Figure 13: Standard deviations of linear acceleration data from the head sea sea-trials (red dots), $h_s = 0.1$m head sea simulation (black squares) and $h_s = 1.25$m head sea simulation (black circles), for varying relative surge velocity (u_r).
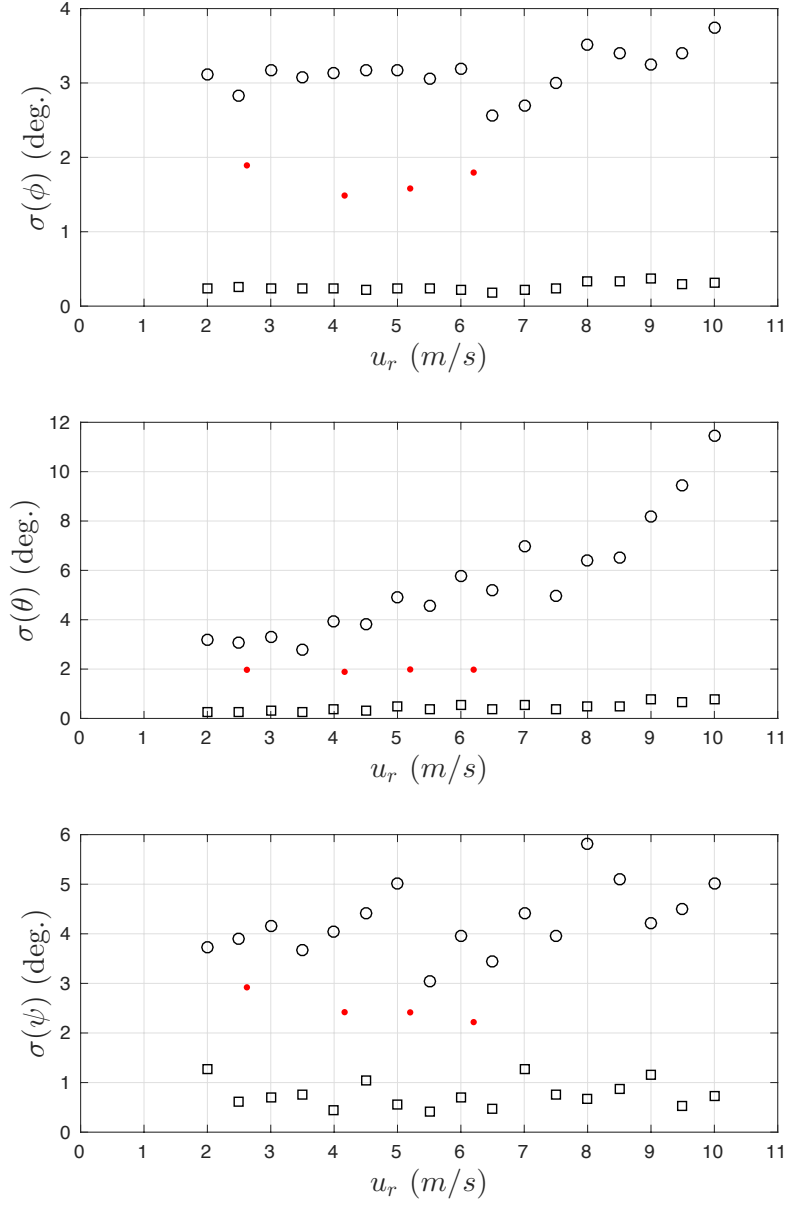
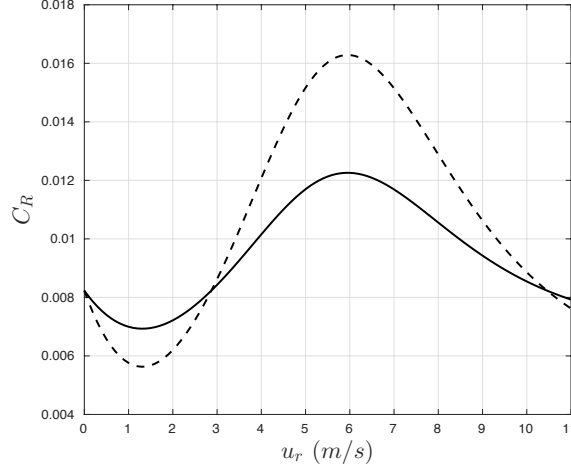Figure 14: Standard deviations of angular displacement data from the head sea sea-trials (red dots), $h_s = 0.1$m head sea simulation (black squares) and $h_s = 1.25$m head sea simulation (black circles), for varying relative surge velocity (u_r).

Figure 15: Residual resistance coefficient (C_R) variation with relative surge velocity (u_r) for the predicted variation (dashed line) and the modified variation (thick line).

However, as will be discussed, the predicted residual resistance curve needed to be modified. In the following, the procedure for determining the surge resistance model parameters from the sea-trials data will be outlined.

Firstly, for a vessel moving at constant speed the propulsive forces in surge are equal to the resistance forces in surge, such that:

$$T_p(u_r) - \frac{X_{D_n}(u_r)}{2} = \rho_{\mathrm{w}} \left[D^4 K_T^{\{3\}} n_p^2 + D^3 u_r K_T^{\{2\}} n_p + D^2 u_r^2 K_T^{\{1\}} \right] - \frac{X_{D_n}(u_r)}{2} = 0, \qquad (45)$$

where T_p denotes the thrust produced by a single propeller defined in (37) and X_{D_n} is surge resistance defined in (34). Note that the vessel has two propellers and it is assumed that the force produced by each propeller is equal to half of the surge resistance force at constant speed. Equation (45) represents a quadratic equation in terms of the propeller shaft speed n_p for different relative surge velocities u_r. All the propeller model parameters are known and therefore the only free variable in (45) is surge resistance. Parameterising the surge resistance model and solving (45) for propeller shaft speed n_p for varying relative surge velocity u_r provides a plot of u_r versus n_p. Therefore, the final step is to choose C_x, C_R and α such that the plot of propeller speed against relative surge velocity correlates with the four data points from the head sea sea-trials. The black dashed line in Figure 16 represents the output of the surge resistance model calibration procedure that has been outlined. It can be seen that it correlates well with the four data points from the sea-trials. In order to achieve this good correlation the current coefficient was chosen as $C_x = 0.3$, the resistance decay coefficient was chosen as $\alpha = 0.2$ and the predicted residual resistance curve was modified. The predicted and modified residual resistance curves are plotted in Figure 15.

In order to verify the surge resistance model, low Sea State 2 ($h_s = 0.1m$) and high Sea State 3 ($h_s = 1.25m$) simulations were carried out at varying surge velocities and propeller shaft speed data was collected. This data is plotted in Figure 16 where the black squares represent low Sea State 2 simulations and black circles represent high Sea State 3 simulations. It is apparent from the figure that sea state has little effect on the surge resistance and that all simulated data correlates
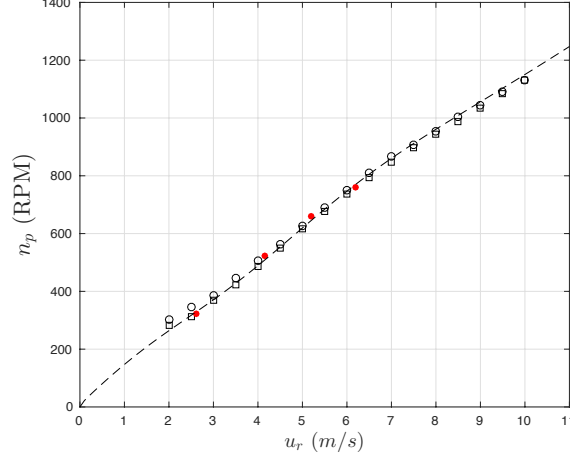
Figure 16: Propeller shaft rotational speed (n_p) vs relative surge velocity (u_r) from the head sea sea-trials (red dots), $h_s = 0.1$m head sea simulation (black squares), $h_s = 1.25$m head sea simulation (black circles) and the surge resistance calibration model (dashed line).

well with the surge resistance model and the sea-trials data.

8.2. Turning circle validation

Four turning circle tests were conducted as part of the sea-trials. Each test attempted to carry out a figure-of-eight manoeuvre with a circular radius of 70 metres and these tests were conducted for near-constant surge velocities of $\approx 2.5m/s$, $\approx 4m/s$, $\approx 5m/s$ and $\approx 6m/s$. Comparative simulations were performed in order to ascertain the rudder lift coefficient gradient $\partial C_L / \partial \alpha$. Note that the rudder zero-lift drag coefficient C_{D0} has been set to zero as this component of surge resistance has been captured in the surge resistance model outlined in the previous section. Two sets of simulations were conducted. In the first set, the rudder angles used in the simulation were made identical to those from the sea-trials at each instance of time. These shall be called open-loop tests. In the second set, the heading angles from the sea-trials were fed to the simulator's autopilot which in turn determined the rudder angles. These shall be called closed-loop tests. In both sets, the forward speed data from the sea-trials were fed to the autopilot in order to determine propeller shaft speed. The sea conditions for all simulations were identical and consisted of a $h_s = 0.1m$ swell-driven sea with no current or local wind.

Without any information regarding the rudders' airfoil geometry, it was not possible to obtain values for the stall angles of the rudders at various Reynolds numbers. It was therefore assumed in the model that the rudders would not experience stall at the maximum deflection angle of $\pm 30°$.

The left column of plots in Figure 17 show the latitude and longitude positions from the turning circle sea-trials and the open-loop simulations. The rudder lift coefficient gradient used to obtain these plots was $\partial C_L / \partial \alpha = 3 \text{ rad}^{-1}$. After a trial-and-error tuning process, this value was deemed to provide a good compromise between the under-turning observed at low speed and the over-turning observed at high speed. It is likely that the simulation does not accurately model the turning dynamics at high forward speed, perhaps not accounting for increased yaw damping or a reduction in rudder lift coefficient due to stall.
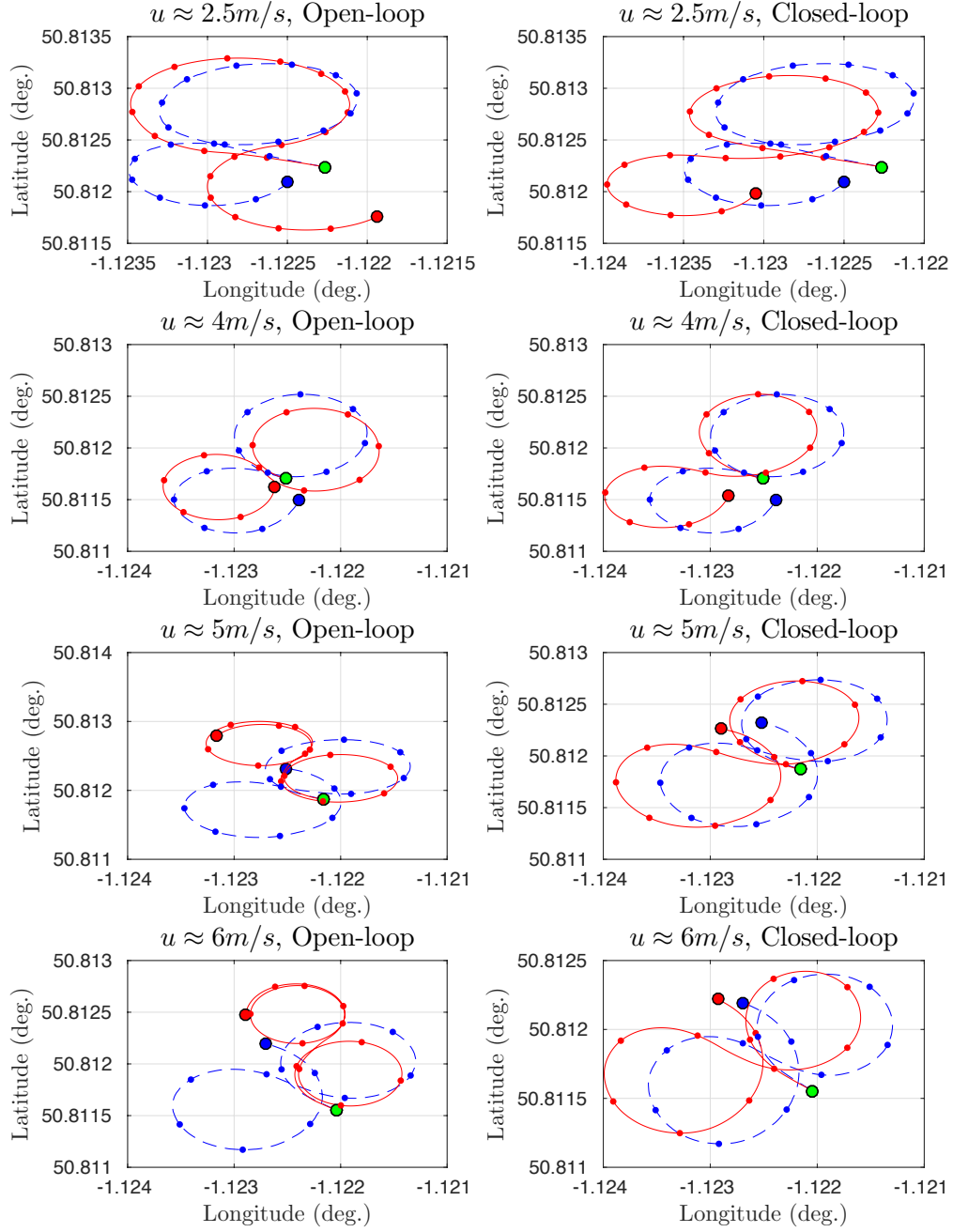
Figure 17: Latitude-Longitude plots of turning circle tests for varying surge velocity (u) from sea-trials (blue dashed line) and simulation (red thick line). The left column of plots are from open-loop simulations and the right column of plots are from closed-loop simulations. Green circles represent the starting positions, blue circles represent the finishing positions of the sea-trials and red circle represent the finishing positions of the simulations. Red ands blue dots represent the locations at ten second intervals.

The right column of plots in Figure 17 show the latitude and longitude positions from the turning circle sea-trials and the closed-loop simulations. It is apparent from these plots that the circular radius of the actual and simulated manoeuvres are very similar for all four surge velocities. There is however a westward drift of the courses taken in the simulations. This is due to small errors in the simulated heading angle which accumulate over time. Figure 18 compares the rudder angles α_r from the sea-trials and the closed-loop simulations. The actual and simulated rudder angle time histories are both quantitatively and qualitatively similar for all surge velocities. However, the simulated rudder angles are noticeably smaller for the $u \approx 6 m/s$ closed-loop test. This is likely to be due to un-modelled turning dynamics at higher speeds.

9. Conclusions

In this paper we have presented a multiphysics simulation model for Halcyon, an unmanned surface vehicle (USV). The simulator consists of a novel wave environment model, a six degree of freedom rigid body dynamics boat model, an actuation dynamics model, an autopilot and an interface with MOOS-IvP - an open-source autonomy management system architecture. The wave environment model generates omnidirectional surface waves which include the effects of ocean swell, local wind, surface current and finite water depth. It achieves this by incorporating two spectral wave models (SWMs) and a current influence spectrum. A nonlinear unified seakeeping and manoeuvring model with fluid memory effects is used to simulate Halcyon's rigid body dynamics. This model is able to capture speed-dependent potential damping and added mass as well as wave-induced forces which makes it an ideal choice for simulating a vessel's dynamics in rough sea conditions.

The vast majority of Halcyon's model parameters were known a priori such as its spatial dimensions, mass and moments of inertia. Its hydrodynamic properties were calculated using the computer program THARBM [4]. Model parameters which were initially unknown were identified by comparing sea-trials data to that from comparable simulations. The first set of comparable simulations involved navigating the vessel into a head sea at near-constant forward speeds. Tuning of the viscous damping matrix and surge resistance model parameters led to good correlations between the simulation and sea-trials data. The second set of comparable simulations recreated turning circle manoeuvres conducted by Halcyon during the sea-trials at different forward speeds in order to identify the lift coefficient gradient of the rudders.

The design and subsequent validation exercises presented in this paper has produced a comprehensive simulation environment to aid in the rapid development of USV autonomy management systems. This simulation tool has the potential to significantly reduce the development time and cost of these systems. However, there are several limitations to the current simulation model. The USV's hydrodynamics could be modelled more rigorously by accounting for planing when calculating the hydrodynamic coefficients; THARBM is only valid for vessels in the displacement or semi-displacement mode. Also, the second-order wave induced forces (wave drift forces) were not included in τ_{wave}. This is due to the lack of a suitable method to predict these forces for a hull form such as Halcyons. Including these unaccounted hydrodynamics will be left for future work. Future work will also be spent on improving the USV's rudder model, namely, identifying the rudders' stall angle to obtain a more accurate lift coefficient gradient. The a priori unknown model parameters were obtained using a manual tuning exercise. Future work will involve developing methods for automating this process such that a certain set of parameters could be identified for suitable USVs using sea trials data. Suitable USVs with a similar shape, configuration and hull form to Halcyon include Shanghai University's 'JingHai-I' [41] and ASV Global's 'C-Target' series [42].
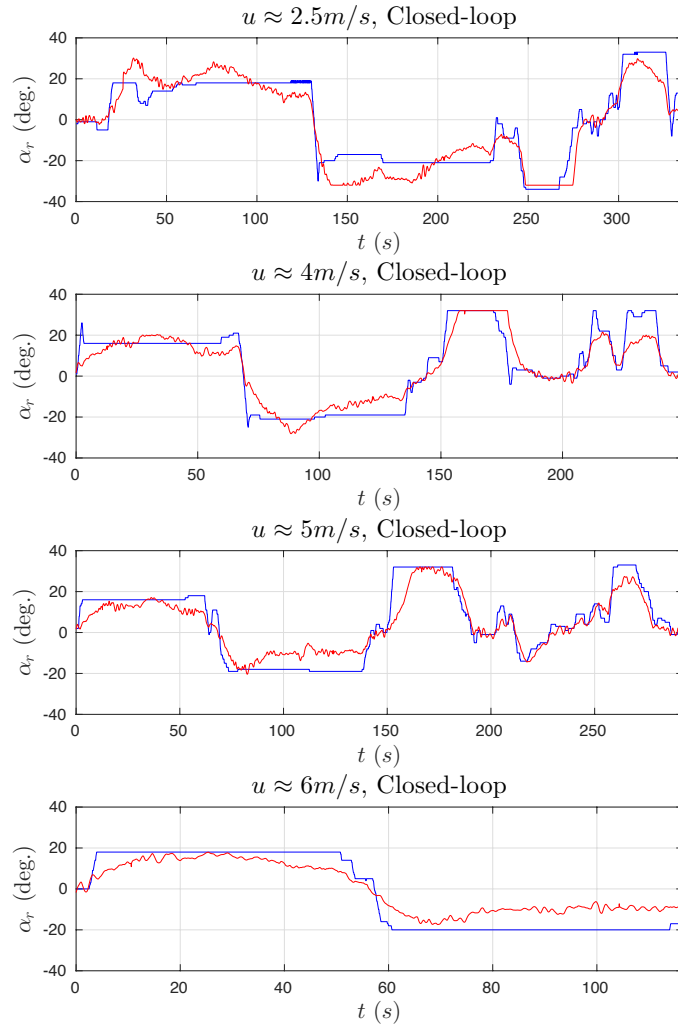
Figure 18: Rudder angle (α_r) vs. time (t) from the turning circle sea-trials (blue lines) and closed-loop simulations (red lines).

Acknowledgements

References

[1] Y. Valeriano-Medina, A. Martinez, L. Hernandez, H. Sahli, Y. Rodriguez, J. R. Canizares, Dynamic model for an autonomous underwater vehicle based on experimental data, Mathematical and Computer Modelling of Dynamical Systems 19 (2) (2013) 175–200.

[2] V. E. Brando, J. L. Lovell, E. A. King, D. Boadle, R. Scott, T. Schroeder, The potential of autonomous ship-borne hyperspectral radiometers for the validation of ocean color radiometry data, Remote Sensing 8 (2).

[3] P. J. Fitzpatrick, Y. Lau, R. Moorhead, A. Skarke, D. Merritt, K. Kreider, C. Brown, R. Carlon, G. Hine, T. Lampoudi, A. P. Leonardi, A review of the 2014 Gulf of Mexico Wave Glider ® field program, Marine Technology Society Journal 49 (3) (2015) 64–71.

[4] D. Hudson, User manual for program suite THARBM, three-dimensional analysis of rigid body motions, Tech. rep., School of Engineering Sciences, Ship Science, University of Southampton (2000).

[5] M. Dunbabin, A. Grinham, Quantifying spatiotemporal greenhouse gas emissions using autonomous surface vehicles, Journal of Field Robotics 34 (1) (2017) 151–169.

[6] D. A. Real-Arce, C. Barrera, J. Hernandez, O. Llinas, Ocean surface vehicles for maritime security applications (The PERSEUS project), in: MTS/IEEE OCEANS 2015 - Genova, 2015.

[7] F. Chen, H. Xiong, J. Fu, The control and simulation for the ADRC of USV, in: Chinese Automation Congress (CAC), 2015.

[8] J. Jiu-Cai, Z. Jie, S. Feng, Modelling, manoeuvring analysis and course following for two unmanned surface vehicles driven by a single propeller and double propellers, in: 27th Chinese Control and Decision Conference (CDC), 2015.

[9] M. Kurowski, E. Rentzow, S. Ritz, B. Lampe, T. Jeinsch, Modelling and control of ASV acting as communication node for deep-sea applications, in: 10th IFAC Conference on Control Applications in Marine SystemsCAMS, 2016.

[10] D. Mu, Y. Zhao, G. Wang, Y. Fan, Y. Bai, USV model identification and course control, in: Sixth International Conference on Information Science and Technology, Dalian, China, 2010.

[11] C. R. Sonnenburg, C. A. Woolsey, Modelling, identification, and control of an unmanned surface vehicle, Journal of Field Robotics 30 (3) (2013) 371–398.

[12] T. I. Fossen, Nonlinear unified state-space model for ship maneuvering and control in a seaway, International Journal of Bifurcation and Chaos 15 (9) (2005) 2717–2746.

[13] M. R. Benjamin, H. Scmidt, P. Newman, J. L. Leonard, An overview of MOOS-IvP and a user guide to the IvP Helm - release 13.5, Tech. rep., Department of Mechanical Engineering, Computer Science and Artificial Intelligence Laboratory, MIT, USA (2013) [cited 26.07.2016]. URL http://oceanai.mit.edu/moos-ivp-pdf/moosivp-helm.pdf

[14] T. I. Fossen, Handbook of Marine Craft Hydrodynamics and Motion Control, Wiley, 2011.

[15] G. B. Whitham, Linear and Nonlinear Waves, John Wiley and Sons, 1974.

[16] T. Elfouhaily, B. Chapron, K. Katsaros, A unified directional spectrum for long and short wind-driven waves, Journal of Geophysical Research 102 (C7) (1997) 15781–15796.

[17] E. Bouws, H. Gunther, W. Rosenthal, C. L. Vincent, Similarity of the wind wave spectrum in finite depth: 1. spectral form, Journal of Geophysical Research 90 (C1) (1985) 975–986.

[18] K. Torsethaugen, S. Haver, Simplified double peak spectral model for ocean waves, in: ISOPE 2004 Touson, France., 2004.

[19] M. K. Ochi, E. N. Hubble, Six-parameter wave spectra, Coastal Engineering Proceedings (15) (1976) 301–328.

[20] O. Nwogu, Effect of steady currents on directional wave spectra, in: International Conference on OMAE; Volume I, Offshore Technology, ASME, 1993, pp. 25–32.

[21] A. A. Mouche, D. Hauser, V. Kudryavtsev, Radar scattering of the ocean surface and sea-roughness properties: a combined analysis from dual-polarizations airborne radar observations and models in C band, Journal of Geophysical Research 111 (2006) 1–18.

[22] F. Nougier, S. T. Grilli, C.-A. Guerin, Nonlinear ocean wave reconstruction algorithms based on simulated spatiotemporal data acquired by a flash LIDAR camera, IEEE Transactions on Geoscience and Remote Sensing 52 (3) (2014) 1761–1771.

[23] K. Hasselmann, T. P. Barnett, E. Bouws, H. Carlson, D. E. Cartwright, K. Enke, J. A. Ewing, H. Gienapp, D. E. Hasselmann, P. Kruseman, A. Meerburg, P. Miller, D. J.Olbers, K. Richter, W. Sell, H. Walden, Measurements of wind-wave growth and swell decay during the joint north sea wave project (JONSWAP), Ergnzungsheft zur Deutschen Hydrographischen Zeitschrift Reihe, A(8) (Nr. 12) (1973) 95.

[24] M. S. Longuet-Higgins, D. E. Cartwright, N. D. Smith, Observations of the directional spectrum of sea waves using the motions of a flotation buoy, in: Ocean Wave Spectra, Prentice Hall, Englewood Cliffs, N. J., 1963, pp. 111–136.

[25] K. E. Kaasen, Time domain model representations of standard wind gust spectra, in: Proceedings of the Ninth International Offshore and Polar Engineering Conference, Brest, France, May 30-June 4, 1999, pp. 74–78.

[26] T. I. Fossen, Guidance and Control of Ocean Vehicles, John Wiley and Sons, 1994.

[27] W. Blendermann, Parameter identification of wind loads on ships, Journal of Wind Engineering and Industrial Aerodynamics 51 (3) (1994) 339–351.

[28] SNAME, Nomenclature for treating the motion of a submerged body through a fluid, Tech. Rep. Technical and Research Bulletin No. 1-5, The Society of Naval Architects and Marine Engineers (1950).

[29] W. E. Cummins, The impulse response function and ship motions, Tech. Rep. 1661, David Taylor Model Basin, Hydromechanics Laboratory (1962).

[30] E. Kristiansen, A. Hjulstad, O. Egeland, State-space representation of radiation forces in time-domain vessel models, Ocean Engineering 32 (2005) 2195–2216.

[31] T. Perez, T. I. Fossen, A Matlab tool for parametric identification of radiation-force models of ships and offshore structures, Moelling, Identification and Control MIC-30(1) (1) (2009) 1–15.

[32] E. V. Lewis (Ed.), Principles of Naval Architecture, 2nd Edition, Society of Naval Architects and Marine Engineers (SNAME), 1989.

[33] O. M. Faltinsen, Sea Loads on Ships and Offshore Structures, Cambridge University Press, 1990.

[34] S. F. Hoerner, Fluid Dynamic Drag, Hartford House, 1965.

[35] J. D. Anderson, Fundamentals of Aerodynamics, 4th Edition, McGraw-Hill, 2007.

[36] M. M. Bernitsas, D. Ray, P. Kinley, K_T, K_Q and efficiency curves for the Wageningen B-series propellers, Tech. Rep. 237, Department of Naval Architecture and Marine Engineering, College of Engineering, The University of Michigan (May 1981).

[37] P. Newman, mex-moos: a Matlab interface for MOOS:V10 communications [cited 05.08.2016]. URL https://github.com/themoos/mex-moos

[38] K. J. Aström, R. M. Murray, Feedback Systems: An Introduction for Scientists and Engineers, v2.10e Edition, Princeton University Press, 2011.

[39] J. van Amerongen, P. G. M. van der Klugt, H. R. van Nauta Lemke, Rudder roll stabilization for ships, Automatica 26 (4) (1990) 679–690.

[40] J. Robinson, Performance prediction of chine and round bilge hull forms, in: Internation Conference, Hydrodynamics of high speed craft, London, Royal Institution of Naval Architects, 1999.

[41] Y. Peng, Y. Yang, J. Cui, X. Li, H. Pu, J. Gu, S. Xie, J. Luo, Development of the USV 'JingHai-I' and sea trials in the Southern Yellow Sea, Ocean Engineering 141 (2017) 186–196.

[42] ASV products [cited 27.01.2017]. URL https://asvglobal.com/products